Unsteady RANS-based DMD Analysis of Airfoil NACA0015 with Gurney Flap

José A. Moríñigo[1,Ŧ], Pablo Anaya-Ruíz [2], Andrés Bustos[1], Rafael Mayo-García[1]

[1] Dept. de Tecnología, CIEMAT
Av. Complutense 40, Madrid 28040, Spain

[2] Universidad Carlos III de Madrid
Av. de la Universidad 30, 28911 Leganés, Spain

[Ŧ] Corresponding author. E-mail: josea.morinigo@ciemat.es

Abstract. The present investigation summarizes the numerical prediction and DMD analysis of the flow in the vicinity of a Gurney flap set on an airfoil NACA0015 at Re=10,300 tested in a water tunnel with time-resolved Particle Image Velocimetry. A series of two-dimensional U-RANS simulations has been accomplished using an incompressible, time-accurate solver of OpenFOAM. A purely data-based DMD analysis has followed to extract the spatio-temporal coherent structures from the time-evolving flowfields, to mimic the experiments. It is stressed that this work focuses on the analysis of this kind of flap by applying DMD to datasets generated with numerical simulations, which has not been previously investigated, but using experimental datasets. Under this approach, the comparison of the numerics with the experimental counterpart shows a remarkable agreement for both the structures and major frequencies, which stresses the suitability of the incompresible U-RANS approach in this class of studies. Special attention has been focused on the modelling of the experimental facility, and a quantification of the prediction accuracy is provided by assessing the deviation of the spectral content. The simulations clearly show the key role of having a good characterization of the water tunnel to be successful at capturing the spectrum and flow unsteadiness. Furthermore, they reveal quite promising for those industrial oriented simulations, which deal with lift-enhancement devices and lift-to-drag ratio optimization of airfoils since they permit an accurate prediction.

Keywords: DMD, Gurney flap, OpenFOAM, Unsteady RANS.

1- INTRODUCTION

Understanding the underlying, complex flow dynamics of airfoils (i.e., turbines for wind and power generation, aircraft wings,...) is a difficult task due to the interplaying phenomena, which occur in a wide range of spatio-temporal scales: boundary layer separation, recirculating bubbles, wakes, turbulence and reacting flow, to cite some important ones. This complexity has led to a strong interest in the reduced-order modelling, to decompose the flow into a set of coherent structures, thus enabling to express the unsteady behaviour as a simpler problem based on modal information, which, as a result, leads to a more affordable representation of the underlying physics. Various algorithmic tools have appeared in the last decades to gain insight into the spectral content and these dominant flow features in time-evolving flows. That is the case of the Principal Orthogonal Decomposition (POD, also known as Principal Component Analysis (PCA), of applicability in other fields besides fluid dynamics); or the Dynamic Mode Decomposition (DMD) technique. See [1-4] for a recent review of the various mode analysis techniques, specifically DMD.

Application of DMD and POD to a diverse class of turbulent flows may be found in the literature: shallow flow [5]; jets [6-13]; mixing layer [14,15]; boundary layer [16-19]; channel flow [20,21]; wake [22-28]; cavity flow [29-33]; flow in tubes [34]; flow around airfoils [35-39], to cite some relevant flows.

At extracting coherent structures from fluid flows, two major approaches may be followed: the exploitation of non-intrusive experimental measurements (e.g., based on time-resolved Particle Image Velocimetry, in short PIV); or by performing high accuracy numerical simulations.

Regarding the first group, several studies have been conducted using DMD and POD methods against time-resolved PIV data, to accurately assess the spectral information in problems with complex flow structures, flow regimes and bifurcations. Hence, in [28] the authors analyse the vortex dynamics of a circular cylinder wake by means of POD. That work follows a methodology closely linked to [35], which instead applies DMD to the airfoil NACA0015 with a Gurney flap setting. The power of the modal analysis is more recently shown in [38], which focuses on the appearance of Görtler vortices in a multi-element airfoil. A comparison of how POD and DMD perform in the case of the lid-driven cylindrical cavity at a variety of Reynolds numbers is given in [33], to identify bifurcation points of the flow.

On the contrary, another group of investigations exploit high-fidelity numerical simulations, as it is the case of Direct Navier-Stokes (DNS) simulations [20,33] to build the spatio-temporal representation needed by DMD and other modal tools.

The present investigation belongs to the second group and focuses on the unsteady flowfield left by an airfoil NACA0015 modified with a Gurney flap (in short GF), which is a passive flow control device, which consists of a short flat plate perpendicularly attached to the pressure side of the airfoil near its trailing edge. Hence, the DMD technique is used to extract valuable information out of time-accurate numerical simulations.

The GF, intended to increase the lift (at the cost of incurring into a drag penalty) and to enhance the lift-to-drag ratio of airfoils, has been applied in a variety of devices since it combines effectiveness with simplicity. Common usages have been in wind energy blades [40-43], helicopter stabilizers or ailerons in race cars [44,45]; and more recently tested in rather demanding aeronautical devices, as rotary-wings and jet turbine blades [46-48]. Interestingly, some concepts based on virtual GFs [49], which mimic the effect of a physical GF by enforcing local ionization of the flow with a plasma actuator near the trailing edge, have been investigated. Further details and a review of the GF technology may be found in [47, 48, 50, 51].

Being the GF geometrical optimization of paramount importance to attain a competitive plus of performance, an accurate prediction of its aerodynamic contribution to the device is a must. To this regard, the developing structures and their unsteadiness dependence on the GF geometry and setting on the airfoil have been analyzed numerically [52,53] and experimentally [54]. Then, the understanding of how they act on the flow dynamics by shedding vortices into the wake, is of major concern to improve the airfoil design.

To the authors' knowledge, there is only the research [35], which applies DMD to the study of the vortex shedding downstream the GF set on an airfoil. Some authors have studied purely the aerodynamics performance attained with GFs, experimentally [54] or numerically. In this respect, a parametric, numerical study of the effect of the GF geometry set on a wind turbine airfoil is conducted with a steady 2D Reynolds Averaged Navier-Stokes (RANS) simulation at Reynolds $Re=2\times10^6$ in [43]. In [45] a steady 3D RANS modelling approach has been followed to analyse the performance of a GF set on the front wing of an F1-racing car. Another steady 3D RANS simulation of a horizontal wind turbine for two configurations of GFs is summarized in [42], computed with OpenFOAM [55]. All these studies relying on steady-state simulations have been accomplished with different eddy viscosity closures for the turbulence modelling.

An interesting, numerical piece of work closely related to the present investigation, is carried out by Meena *et al.* in [52], where a flat plate and three symmetrical NACA airfoils (0006, 0012 and 0018) at $Re=1000$, have been simulated with varying GF settings. They use incompressible DNS under 2D and 3D assumptions, to discuss the dependence of the flow major frequencies

on the angle of attack. Meena *et al.* show that the vortical structure dynamics are driven by the GF geometry. In [53] the dependence of the wake unsteadiness of an HQ17 airfoil at $Re=10^6$ is numerically explored for various GF configurations, mostly using 2D Unsteady RANS (U-RANS) simulations. The authors characterize the mean lift and drag coefficients of each GF geometry analyzed, as well as provide the major flow frequency, which arises from the simulations.

The interplay between the geometrical definition of the GF and the resulting spectral content in the wake has been scarcely studied until the present. Hence, the present investigation put its emphasis on the predictability of this phenomenon using datasets from U-RANS simulations as input to the DMD algorithm, to extract the dominant flow modes.

In particular, this work shows the accurate numerical prediction of the dominant flow modes which originates for the airfoil NACA0015 with a GF setting, which has been experimentally studied in [35]. A series of incompressible, turbulent 2D U-RANS simulations carried out with OpenFOAM have clearly shown the right capturing of the time-evolving structures when the confinement of the flow in the water tunnel test-section and an adequate turbulence characterization are taken into account. The numerical-experimental comparison stresses the correctness of the U-RANS approach and very good matching with the mentioned experiments. The data postprocessing using the DMD tool reveals that it is plausible to successfully extract the major flow modes, to provide a reduced order representation of the flow dynamics.

The rest of this article is structured in what follows. Section 2 provides the description of the experimental facility and tested airfoil. Then, section 3 summarizes the numerical approach followed to produce the flow data, with an emphasis on the grid, turbulence modelling and computational domain independence. The next section introduces the DMD mathematics and the data processing workflow. In section 5, the results are presented and discussed. Finally, conclusions are given in section 6.

2. EXPERIMENT DESCRIPTION

This section summarizes the experiment and data [35], which provide fundamental information to accomplish the present numerical study.

2.1 Water channel

The facility where the experiment was carried out is a low-speed water tunnel with a working section of 600 x 600 x 3000 mm (height x width x length), according to [35]. A further description of the facility may be found in [56, 57]. The incoming free-stream velocity at the inlet

of the working section was U_∞=52 mm/s with a turbulence intensity of about Tu=0.8%. Such free-stream turbulence level corresponds to the rather homogeneous wake left by a grid array of wires. The airfoil inside the test section is horizontally placed at approximately half the height of the test cross-section, as depicted in Fig. 1. The tunnel has the capability of timeline visualization with both dye injection and hydrogen bubble curtains emission using platinum filaments. By these means, it is ensured that the flow around the airfoil has no noticeable separation. Also, it permits the investigation of the boundary layer and wake flow.

2.2 NACA0015 with Gurney flap

The tested NACA0015 airfoil has a chord length of c=200mm and it spans the width of the water tunnel cross-section, which is 600mm and has end plates on both sides. Because of manufacturing simplicity, the trailing edge (TE) has a thickness of 2mm. The airfoil is positioned at zero angle of attack. The GF height is h=5mm (2.5%c), of 1mm thickness, and its leading wall is set at 10%c ahead of the TE. See Fig. 2 for the corresponding geometry definition. The Reynolds number referred to its chord and test velocity U_∞=52 mm/s is $Re=\rho U_\infty c/\mu$=10,300.

2.3 Data

Time resolved 2D PIV measurement was taken in the xy-plane of the airfoil (the streamwise centreplane of the tunnel). Details of the PIV system may be found in [35] and are not repeated here. Two streamwise regions (denoted Region I & II in Fig. 3) placed in the wake zone were measured individually, so a large number of snapshots of the instantaneous velocity field were recorded for each region and later analysed with DMD. The systematic error of the velocity measurement was estimated to be 1% according to [58]. Besides the PIV data, the instantaneous vortices visualization identifies a von Kármán street in the wake, visible in Fig. 3. The dynamic modes built with the DMD algorithm applied to the PIV data, has permitted to characterize the flowfield in terms of structures and major spectral content. This PIV-based DMD-processed data constitutes the experimental reference for the present work, to assess the numerical-experimental DMD comparison, which is summarized in the results section.

3. SIMULATION APPROACH

3.1 Numerical solver

The incompressible U-RANS equations are solved using the finite volume formulation provided by the OpenFOAM v.8 framework. A 2nd-order spatial linear upwind scheme with implicit

2nd-order backward time integration gives an adequate spatio-temporal resolution of the flow, modeled as 2D in the present approach.

The *pisoFOAM* solver implements a pressure-based formulation for the pressure-velocity calculation of the U-RANS equations. It uses the *Pressure Implicit with Splitting of Operators* (PISO) algorithm [55,59] to partially decouple operations on velocity from those on pressure. It involves one predictor step and two (pressure-) corrector steps per time-step, to recover the solenoidal nature of the velocity field (divergence-free), needed for mass conservation in each finite volume.

Flow solution at each time step is attained with a Preconditioned Gradient Conjugate (PCG) iterative method. The costly corrector steps for the pressure variable are preconditioned with a simplified diagonal-based Incomplete Cholesky factorization scheme on the PCG solver. In addition, the diagonal-based Incomplete LU factorization preconditioning on the PBiCG solver is applied for the rest of the variables (momentum and turbulence). The under-relaxation factor is set to 0.7 for all variables. The absolute tolerance is prescribed to be 10^{-6} for each variable per time step.

3.2 Turbulence modelling

The k-ε Eddy Viscosity Model (EVM) is one of the most popular, widely used turbulence closures for the U-RANS equations and it continues as a workhorse of the CFD industry at present [60,61]. Turbulence transport equations are solved for two scalar properties of turbulence: the k-equation, which models the transport of the turbulent kinetic energy; and the ε-equation, which models the dissipation rate of the turbulent kinetic energy. OpenFOAM implements various k-ε closures. Among them, there are four low-Reynolds EVMs which predict the turbulence behaviour in the vicinity of the walls and, as a result, demand very fine cells in the near wall regions (that is, their low-Reynolds formulation fulfils the non-dimensional wall distance y^{+}~1 condition): Launder & Sharma [62], Lien & Leschziner [63], Lam & Bremhorst [64] and the non-linear EVM of Lien, Chen & Leschziner [65]. It is noticed that other closures intended for y^{+}>>1 are available in OpenFOAM, as well as some modified EVMs (as the k-ω Shear Stress Transport model [66], of widespread use), but whose implementation departs from the original formulation. These ones are not used in this study.

The EVM of Launder & Sharma is taken as the baseline for the turbulence modelling in the present investigation and its prediction is compared with the other abovementioned models (see subsection 3.4) to support this approach. The Launder & Sharma EVM is devised to agree in those classes of fluids corresponding to free shear-layer and wall bounded flows, both with

relatively small pressure gradients, then it is a priori suited to the flow under study. Its accuracy degrades as the adverse pressure gradient becomes larger [67]. The incompressible Navier-Stokes equations read

$$\frac{\partial u_j}{\partial x_j} = 0$$

$$\frac{\partial u_i}{\partial t} + \frac{\partial (u_j u_i)}{\partial x_j} = -\frac{\partial}{\partial x_i}\left(\frac{p}{\rho_0}\right) + \frac{\partial}{\partial x_j}\left[\nu\left(\frac{\partial u_i}{\partial x_j} + \frac{\partial u_j}{\partial x_i}\right)\right]$$

(1)

being u_i the *i*-component of the fluid velocity, *p* the pressure, ρ_0 the fluid density (constant) and *v* the viscosity of the fluid. The assumption of velocity and pressure expressed as the sum of a mean and a fluctuation, leads to u = $\bar{u}$ + u', p = $\bar{p}$+ p' , then the U-RANS equations follow

$$\frac{\partial \bar{u}_i}{\partial t} + \frac{\partial (\bar{u}_j \bar{u}_i)}{\partial x_j} = -\frac{\partial}{\partial x_i}\left(\frac{\bar{p}}{\rho_0}\right) + \frac{\partial}{\partial x_j}\left[\nu\left(\frac{\partial \bar{u}_i}{\partial x_j} + \frac{\partial \bar{u}_j}{\partial x_i}\right) - \overline{u'_i u'_j}\right]$$

(2)

where $-\overline{u'_i u'_j}$ is the Reynolds stress term.

The Reynolds stress term is modelled with the Boussinesq stress-strain relationship

$$-\overline{u'_i u'_j} = -\nu_t\left(\frac{\partial u_i}{\partial x_j} + \frac{\partial u_j}{\partial x_i}\right) + \frac{2}{3}k\delta_{ij}$$

(3)

being *k* the turbulent kinetic energy and δ_{ij} the Kronecker delta function. The combination of (2) and (3) leads to the implemented version of U-RANS in OpenFOAM

$$\frac{\partial u_i}{\partial t} + \frac{\partial (u_j u_i)}{\partial x_j} = -\frac{\partial}{\partial x_i}\left(\frac{\tilde{p}}{\rho_0}\right) + \frac{\partial}{\partial x_j}\left[(\nu + \nu_t)\left(\frac{\partial u_i}{\partial x_j} + \frac{\partial u_j}{\partial x_i}\right)\right]$$

$$\tilde{p} = \bar{p} + \frac{2}{3}\rho_0 k\delta_{ij}$$

(4)

where the redefined pressure variable includes the isotropic part of the Reynolds stress term; ν_t is the eddy (turbulent) viscosity; and the mean velocity is now written without the hat symbol. The closure of these equations with the Launder & Sharma *k-ε* model reads

$$\frac{\partial k}{\partial t} + \frac{\partial (u_j k)}{\partial x_j} = \tau_{ij}\frac{\partial u_j}{\partial x_j} - \varepsilon + \frac{\partial}{\partial x_j}\left[\left(\nu + \frac{\nu_t}{\sigma_k}\right)\frac{\partial k}{\partial x_j}\right] + 2\nu\left(\frac{\partial \sqrt{k}}{\partial x_j}\right)^2$$

(5a)

$$\frac{\partial \varepsilon}{\partial t} + \frac{\partial (u_j \varepsilon)}{\partial x_j} = C_{\varepsilon 1}f_1\frac{\varepsilon}{k}\tau_{ij}\frac{\partial u_j}{\partial x_j} - C_{\varepsilon 2}f_2\frac{\varepsilon^2}{k} + \frac{\partial}{\partial x_j}\left[\left(\nu + \frac{\nu_t}{\sigma_\varepsilon}\right)\frac{\partial \varepsilon}{\partial x_j}\right] + 2\nu\nu_t\left(\frac{\partial^2 \varepsilon}{\partial x_j^2}\right)^2$$

(5b)

$$\tau_{ij} = 2\nu_t S_{ij} - \frac{2}{3}k\delta_{ij} \quad , \quad S_{ij} = \frac{1}{2}\left(\frac{\partial u_i}{\partial x_j} + \frac{\partial u_j}{\partial x_i}\right) \tag{5c}$$

being the eddy viscosity defined by

$$\nu_t = C_\mu f_\mu \frac{k^2}{\varepsilon} \tag{6}$$

The rest of parameters set in this EVM are $C_{\varepsilon 1}$ =1.44, $C_{\varepsilon 2}$ =1.92, σ_k=1.0, σ_ε=0.7194, f_1=1.0 and the damping functions

$$f_2 = 1 - 0.3exp(-Re_t{}^2) \quad , \quad f_\mu = exp\frac{-3.4}{(1 + Re_t/50)^2} \quad , \quad Re_t = \frac{k^2}{\nu\varepsilon} \tag{7}$$

The coefficients provided for this closure are empirical relations fitted for some families of flows. This has motivated that some authors examine its recalibration [68,69] to improve its prediction. The implementation of (5) in OpenFOAM exploits the change of variable [70]

$$\varepsilon^* = \varepsilon - 2\nu\left(\frac{\partial\sqrt{k}}{\partial x_j}\right)^2 \tag{8}$$

Variable ε^* permits to simplify the setting of the dissipation rate at the walls, being ε^*=0 (as for the turbulent kinetic energy, which is k=0 at the walls). Setting the turbulence quantities at the domain inlet implies the estimation of the turbulent kinetic energy and its dissipation rate at the water tunnel inlet

$$k_{inlet} = \frac{3}{2}\left(\frac{Tu(\%)}{100}\right)^2 U_\infty^2 \quad , \quad \varepsilon_{inlet} = C_\mu{}^{3/4}\frac{k^{3/2}}{l} \tag{9}$$

where $Tu(\%)$ is the turbulence intensity, C_μ=0.09, l=0.07c, and U_∞=52mm/s is the mean velocity at the tunnel inlet according to the experimental setup [35].

3.3 Computational domains

Two gridded 2D computational domains have been built. One mimics the airfoil in free-flight, where the domain extension is truncated into a finite region (see Fig. 4a). Its outer contour is set far away to guarantee the flowfield insensitivity to the boundary condition (BC) location. The second computational domain (Fig. 4b) corresponds to the airfoil mounted inside the water tunnel, thus mimicking the performed experiment (the distance to the tunnel walls and inlet matches the facility dimensions). In this domain setup, similarly to the free-flight case, the outlet

boundary is set at 80c downstream the trailing edge of the airfoil, to enforce the flowfield insensitivity to the domain extension, as well.

The generation of hybrid hexahedra/prism -based grids has been the preferred option because of their quality and high skewness control. It should be noticed that the hexahedra/prism nomenclature is due to OpenFOAM handles 3D grids in a strict sense, even at doing 2D simulations. Then, the 2D cells (xy-plane) are extruded with a constant depth (here fixed at 1mm) along the z-axis, thus building 3D cells. First, the gridding around the airfoil and in Regions I & II has been done with hexahedral cells (colored in yellow in the zoomed view of Fig. 5a). This hexahedra-based zone exhibits identical topological blocking and gridding in both computational domains, filling a fixed portion of the complete grid. Then, a clearer comparison of the results will be possible. Secondly, an unstructured prism-based grid has been built in the rest of the computational domain, extending from the border of the fixed portion up to the outer boundary of the domain, as can be seen in Fig. 5. Consequently, this prism-based grid differs in both domains, being specific of each one.

Another important aspect, besides the above mentioned insensitivity to the domain extension, is the definition of an adequate grid density across the domain, with an emphasis on the vicinity of the airfoil, resolution of boundary layers, GF, TE and near wake. Such density must guarantee the grid independence of the results. A standard procedure of doubling and halving the grid density in the hexahedra-based zone has been accomplished. It has permitted to identify a baseline grid (see Table 1 for its size in each zone and the total number of cells) adequate to carry out the series of U-RANS simulations. A posteriori analysis of the computed flowfields has confirmed that the $y^+<1$ condition is satisfied over the attached flow region of the airfoil wall for all turbulent simulations, hence in agreement with the EVMs requirement. There is consensus that the fulfilment of the above mentioned issues related to the grid quality is of utmost importance to trust the numerics provided by a solver in the simulations.

3.4 Methodology and validation

3.4.1 Execution of simulations

U-RANS simulations have been performed with Δt=10^{-4}s for laminar flow and Δt=5·10^{-5}s for turbulent flow, which provides a rather conservative Courant number < 0.2. To fully develop the flow quasi-periodicity, a time transient of 1000s has been integrated. It means that the BC inlet information is convected across the baseline computational domains more than two times; and that the fluid particles flow along the airfoil chord more than 250 times. Because of the high

computing cost involved and to speed up the simulations, a domain decomposition of the grid has been done in OpenFOAM, parallelized within 40 MPI tasks in the cluster ACME located at CIEMAT [71]. The computing cost per completed U-RANS simulation corresponds to aprox. 20,160 CPU-hours. Thus, the entire champaign of simulations implies a cluster usage of about 221,760 CPU-hours (not including within this figure the initial solver executions needed for the fine setups). Each simulation setup, checkpointed data and corresponding time sequence of flowfields (double-precission numbers) stored and used for their subsequent DMD processing, occupies aprox. 53Gb.

To assess the difference in the results provided by two generic U-RANS simulations in their respective grids, the metric based on comparing the amplitude and spectral content of the airfoil lift and drag coefficients has been adopted.

3.4.2 Extension of the baseline domain

To correctly size the spatial dimension of the computational domain, three domain sizes across the xy-plane have been generated for the free-flight airfoil, with a downstream length: 40, 60 and $80c$; and a corresponding up/downward length: 20, 40, $60c$ (see Fig. 4). The analysis of the unsteady lift and drag coefficients (computed with both laminar flow modelling and U-RANS with the Launder & Sharma EVM) has shown that no noticeable variation of their amplitude, neither the major oscillation frequency, is observed in the two larger domains. Therefore, the larger one (downstream: $80c$; up/downward: $60c$) has been chosen as the baseline domain for all the simulations of the free-flight airfoil. For the water tunnel case, the chosen baseline domain corresponds to an upstream and up/downward lengths sized according to the original tunnel geometry. A downstream length prescribed at $80c$ is defined as in the free-flight baseline domain.

3.4.3 Validation and intercomparison of simulations

The baseline domains of the airfoil in free-flight and inside a water tunnel have been presented in the previous subsection (see also Table 1 and Fig. 5). As part of the grid independence study, two additional grids have been built for the water tunnel baseline domain (only differing in the gridding of the zone close to the tunnel wall). A view of these grids is depicted in Fig. 6: the water tunnel baseline gridded domain is here denoted Grid #1. The other two grids correspond to Grid #2, which has a coarser hexahedra-cells layer by the boundary layer over the tunnel walls (intended for laminar flow simulations); and to Grid #3, which has near isotropic

prism-cells close to the tunnel walls, and it is intended for setting a slip-flow BC on the tunnel walls to eliminate the effect of the developing boundary layers over them.

More importantly, these two additional built Grids #2 & #3 are exploited in the present work to better clarify the effect of the domain type (free-flight vs. water tunnel) and BCs on the flow spectrum. Table 2 shows the combination of the grids plus a BC type (slip-flow BC vs. non-slip-flow BC set on the tunnel walls) to analyse the possible flow confinement effect of an airfoil tested in a tunnel of moderate cross-section size. This issue is discussed in the results section.

In the case of unsteady Navier-Stokes simulation with laminar flow modelling using Grid #1 and Grid #2, identical lift and drag amplitude and spectra for the solution have been obtained. This stresses that both grids are adequate for the prediction of laminar flow in the water tunnel domain. The lower number of cells of Grid #2 implies a less time-consuming simulation.

In the turbulent case, the series of U-RANS simulations performed on Grid #1 with the four EVMs described in subsection 3.2, have shown a very small variation of the airfoil forces amplitude and their spectral information, as can be seen in Tables 4 and 5, respectively. This observed insensitivity to the particular EVM has pointed out to apply the DMD algorithm only to the U-RANS equations coupled to the Launder & Sharma closure, which is taken as the baseline EVM in this investigation.

The comparison of the spectra computed from turbulent and laminar flow modelling in the free-flight and water tunnel domain (this with Grids #1, #2 and #3), is summarized in Table 3.

4. DMD ALGORITHM

Reduced-order modelling is a vast field in which important contributions have been done in the last decades [72,73]. Several techniques have emerged in the meanwhile and, in particular, the DMD is one of those well-developed tools which has become a workhorse algorithm for the data-driven analysis of high-dimensional systems. Compared to the also well-developed POD technique [4] (whose modes contain several frequencies), it may cause a loss of phase information, since the spatial POD modes may be temporarily dependent on each other. On the contrary, DMD provides the dynamic modes with corresponding definite frequencies and captures the persistent flow dynamics over the temporal window of observation. This means that the identified structures of the modes are not linked to the higher energy content. Besides, there is no recurrence of the underlying governing equations, using only a set of snapshots of the flow. It can be said that both techniques are complementary and useful to analyse the flow dynamics. The DMD method was established by Rowley *et al.* [1] and Schmid [3,13] in the fluid

dynamics arena, based on the Koopman operator [2] which simplifies a nonlinear dynamical system as a higher-dimensional linear system. Basically, the DMD technique takes a sequence of nonlinear flow samples and decomposes them into a set of discrete modes, which represent the dynamic characteristics.

4.1 Mathematical background and algorithmic

The basics of the DMD formulation is presented in what follows (see [3,73-75] for further details). In this work, a uniform time step is used to generate the sequence of m snapshots, which correspond to instantaneous flowfields (in general available from experimental data or large-scale numerical simulations). It is noticed that some authors [76] have discussed the idea of non-uniform sampling in time to generate the flow snapshots sequence. This would permit the concatenation of data taken from different experiments or simulations, to build a valid DMD dataset. In matrix notation, the mentioned sequence reads

$$X = \{x_1, x_2, \ldots x_m\} \tag{10}$$

where vector $x_j \in \mathbb{R}^n$ stands for $x(t_j)$ with $j=1,2...m$, corresponding to the j-th flowfield restructured as an n-size column vector. The time step between any two consecutive flowfields is small enough to resolve the smallest frequency of the system dynamics.

It is assumed that a linear mapping $A \in \mathbb{R}^{n \times n}$ connects the flowfield at t_j to the subsequent flowfield at t_{j+1}. Then, $x_{j+1} = Ax_j$ and this mapping is approximately the same over the entire sampling interval. In matrix form, it reads $X' = AX$, with $X' = \{x_2, x_3,... x_{m+1}\}$. The best fit operator A, which closely resembles the Koopman operator, is obtained as

$$A = argmin_A \|X' - AX\|_F = X'X^{\dagger} \tag{11}$$

being $\|\bullet\|_F$ the Frobenius norm and $\dagger$ indicates the Moore-Penrose pseudo-inverse [77]. Typically m≪n, which implies a reduction of dimensionality since there are at most m non-zero singular values (and corresponding singular vectors) in X. This is done without requiring A explicitly. It is possible to approximate X with a truncated Singular Value Decomposition (in short, SVD) [12]

$$X \approx U_r \Sigma_r V_r^T \tag{12}$$

where the SVD provides the first $r \leq m$ singular values and vectors, as indicated by the subindex of the matrix notation. The diagonal matrix Σ_r ($\in \mathbb{R}^{r \times r}$) contains the first, larger r singular values; matrices U_r ($\in \mathbb{R}^{n \times r}$) and V_r ($\in \mathbb{R}^{m \times r}$) are real, unitary matrices whose columns correspond to the

spatial and temporal structures of the flow, respectively. Inserting eqn. (12) into eqn. (11), the full matrix $\boldsymbol{A}$ is

$$A = X'V_r \Sigma_r^{-1} U_r^T \tag{13}$$

The projection of $\boldsymbol{A}$ onto the columns of $\boldsymbol{U_r}$ gives a smaller matrix $\in \mathbb{R}^{r \times r}$ (with the same leading r eigenvalues and eigenvectors), which implies a lower computing cost. This reduced-order matrix reads

$$\widetilde{A} = U_r^T A U_r = U_r^T X' V_r \Sigma_r^{-1} \tag{14}$$

Its spectral decomposition

$$\widetilde{A} W = W \Lambda \tag{15}$$

provides the first r eigenvalues of the full matrix $\boldsymbol{A}$ through the matrix $\boldsymbol{\Lambda} \in \mathbb{R}^{r \times r}$; and the columns of $\boldsymbol{W} \in \mathbb{R}^{r \times r}$ are the eigenvectors of $\widetilde{A}$. It is stressed that $\widetilde{A}$, $\boldsymbol{W}$ and $\boldsymbol{\Lambda}$ are $r \times r$ small matrices. The high-dimensional DMD modes may be reconstructed

$$\boldsymbol{\Phi} = X'V_r \Sigma_r^{-1} W \tag{16}$$

which is a large $n \times r$ matrix that holds the eigenvectors of $\boldsymbol{A}$, then

$$A \boldsymbol{\Phi} = \boldsymbol{\Phi} \Lambda \tag{17}$$

The DMD eigenvalues μ_j (j=1,2,...r), corresponding to matrix $\boldsymbol{A}$, lead to the definition of the continuous eigenvalues $\omega_j = log(\mu_j)/\Delta t$. Hence, the continuous spectral expansion may be written in continuous time as

$$x(t) = \sum_{j=1}^{r} \Phi_j e^{\omega_j t} b_j = \boldsymbol{\Phi} exp(\boldsymbol{\Omega} t)\, \boldsymbol{b} \tag{18}$$

being $\boldsymbol{\Omega}$ a diagonal matrix with the eigenvalues ω_j set in its diagonal; and the vector $\boldsymbol{b}$ initialized out of the first snapshot $\boldsymbol{x}_1$ of the flow sequence, then

$$\boldsymbol{b} = \boldsymbol{\Phi}^{\dagger} \boldsymbol{x}_1 \tag{19}$$

To take into account the energy of each POD mode, a weight linked to the singular values may be built, then the reduced matrix $\widetilde{A}$ may be rewritten as

$$\widehat{A} = \Sigma_r^{-1/2} \widetilde{A} \Sigma_r^{1/2} \tag{20}$$

Its spectral decomposition leads to

$$\widehat{A}\,\widehat{W} = \widehat{W}\,\Lambda \tag{21}$$

And now W exploits the weighting

$$W = \Sigma_r^{1/2}\widehat{W} \tag{22}$$

The modal matrix Φ is calculated again using eq. (16). As a result, the norm of the DMD nodes is not unitary as each mode participates weighted by its corresponding singular value. The energy of the DMD modes is obtained as their Frobenius norm squared.

4.2 Application to U-RANS datasets

The entire flowfield and variables (u, v, p, k and ε) have been saved every 10 milliseconds within the last 10s interval of the baseline U-RANS simulation (that is, from the time instant 990s to 1000s), then providing a collection of 1000 snapshots to be processed by the DMD algorithm. It is the v-component of the velocity vector (u,v) the selected one in this investigation for further comparison with the available corresponding experimental data [35]. Hence, matrix X has been built by linear interpolation of the v-variable into a 32x32 Cartesian grid superimposed on Regions I & II (width=65mm and height=60mm). This step has been repeated for all the snapshots, so the X columns are filled up. Finally, the input to the DMD algorithm are matrices X and X' of size 1024x999. The SVD truncation has been set to r=21, large enough to resolve the dominant modes identified in the experiments (notice that the extraction of PIV data in Regions I & II is done using a rather coarser 16x16 pixelation [35]).

5. RESULTS AND DISCUSSION

The quasi-periodical flow pattern left by the airfoil corresponds to a von Kármán vortex street, whose dynamics have been captured with both the free-flight and water tunnel computational domains. A snapshot of the velocity field in the water tunnel domain is shown in Fig. 7, where the progressive growth of the boundary layer along the tunnel walls and the diffusion of the wake are clearly seen. The gridded region downstream the airfoil permits a sharp resolution of the vortical structures across an extension of about two chords. This region embeds the boxes where PIV datasets have been gathered.

These structures get more and more blurred as convection progresses, because of diffusion caused by the larger size of the cells set farther from the airfoil. It should be mentioned that this higher wake diffusion at large distances attributed to the larger cells, leads to dampening of the interaction at the outlet BC of the domain. Hence, larger cells in this zone of the computational

domain contributes to fighting against spurious wave reflections and artificial synchronization mechanisms that might affect the vortex shedding phenomenon.

In GFs, typically a recirculation bubble appears just ahead of them as sketched in Fig. 8. Depending on the Reynolds number, two flow patterns are possible. In the present case with $Re \sim O(10^4)$, the expected flow pattern corresponds to Fig. 8b, which will be analyzed later. The situation depicted in Fig. 8a corresponds to a pair of shear layers, which extend from both sides of the airfoil and clamp a separation bubble zone. This recirculation encloses two counter-rotating vortices. The mentioned pattern is plausible for low Reynolds flows, or even it can be seen as a time averaged pattern of Fig. 8b; that is, a time-integral of the periodical shedding of spanwise vortices, which was hypothesized in such a way by Liebeck [39] and more recently verified using time-averaged velocity datasets from PIV. The oscillation of the recirculation bubble near the GF occurs typically coupled with the vortex shedding dynamics of the von Kármán street.

5.1 Major frequencies prediction

The capture of the major spectrum content of these vortical structures and recirculating flow is a key aspect of performing a DMD analysis on an accurate dataset. Hence, it is fundamental to quantify the sensitivity of the major flow frequencies to variations in the computational domain and imposed BCs, as well as to the flow modelling in general.

Prior to performing a DMD on the time-evolving flowfield, the frequency content has been analyzed by carrying out an FFT on the drag coefficient of the airfoil, because this provides relevant information about how it depends on the flow modelling. Table 3 provides the prediction of the first (f_0) and second ($2f_0$) frequencies found with laminar and turbulent flow modelling (this last using the Launder & Sharma EVM, described in subsection 3.2). Interestingly, the results clearly point out the substantial dependence with the type of computational domain and BCs imposed. First, laminar flow modelling leads to underpredicting the frequencies by about 20% with regard to its turbulent counterpart in all the scenarios described in Table 3. Second, it is noticed a monotonic shift of the predicted frequencies: they get closer to their empirical counterparts as the fidelity of the computational domain and BCs improves. This observation is typically expected to occur, but Table 3 permits to quantify the incurred deviation for each computational domain considered (it should be noted that often, the precise geometrical details of the facility are unreported, then it contributes to adding uncertainties and a deviation of the numerics).

Hence, the best numerical-experimental agreement occurs for the U-RANS simulation carried out with the water tunnel domain plus non-slip-flow BCs imposed on its walls. In this case, the deviation from the empirical frequencies is bounded within ~1.9% for turbulent modelling.

On the contrary, the setting of slip-flow BCs on the tunnel walls implies a larger departure from the experiments in both laminar (18.4%) and turbulent (4.6%) flow modelling scenarios. The comparison with the experimental frequencies stresses the need of mimicking the experimental facility in a strict sense for having the right capture of the spectrum.

The main difference observed in the flow computed with both U-RANS simulations performed with/without a non-slip-flow BC set on the tunnel walls is the appearance/disappearance of boundary layers over the tunnel walls. Hence, it suggests that the added flow constriction due to the developing boundary layers through the test-section of the airfoil imparts a slight blocking effect, which is responsible for increasing the major oscillating frequency and superharmonics that develop.

The power spectrum of the airfoil time-dependent forces (lift and drag) has been also computed with laminar and turbulent flow modelling in the water tunnel domain with non-slip-flow BCs (it is shown in Fig. 9 for the drag coefficient). Interestingly, the power spectrum reveals very definite frequencies and negligible noise level. It is also visible the above mentioned underprediction given with laminar flow modelling, and also it shows that there is an indiscernible energy content in superharmonics higher than the second one ($2f_0$), in contrast to the power spectrum built using DMD modes, as it will be shown later in this section.

5.2 Sensitivity to the EVMs and turbulence intensity

The prediction of the major spectrum frequencies provided by the U-RANS (Launder & Sharma EVM) simulation in the water tunnel domain results to be remarkably accurate. But a question arises about the sensitivity of the computed spectrum to the selected turbulence closure in the U-RANS simulation. To clarify this point, an identical U-RANS simulation has been repeated for the other three low-Reynolds EVMs available in OpenFOAM, that is: Lien & Leschziner; Lam & Bremhorst; and the non-linear EVM (NLEVM) of Lien *et al.* (see subsection 3.2). Table 4 summarizes the computed major frequencies. Even with the non-linear EVM of Lien *et al.*, the frequency prediction differences are quite small (the NLEVM bounds the deviation at ~0.9%). The mean value and oscillation range of the lift and drag coefficients are provided in Table 5 for comparison purposes. The quite small departure among predictions suggests the adequacy of

the Launder & Sharma closure for accurate simulation of this class of flow. Thus, it has been adopted as the baseline turbulence closure in this investigation.

Another important issue is the turbulence characterization at the tunnel domain inlet and how it may affect the computed spectrum. The conducted experiment in the water tunnel facility corresponds to an intensity of about Tu~0.8%. In this work, a series of U-RANS simulations with the Launder & Sharma EVM and varying Tu has been conducted to quantify to which extent an intensity shift (translated into the k and ε BCs setting) modifies the major tone of the spectrum. This effect is summarized in Fig. 10 for the simulations at Tu=0, 0.4, 0.8 (baseline) and 1.6%. There is a rather flat curve for Tu >~0.6% that shows the, somehow, insensitiveness of the computed f_0 to Tu within this interval. Besides, it can be seen that the major frequency f_0 decreases as the turbulence intensity decreases. In particular, the frequency approaches the value f_0~0.55Hz at $Tu\rightarrow0$, such that the laminar flow modelling spectrum is recovered (slightly overestimated). Then, a consistent behaviour is obtained.

A time sequence of velocity flowfields over one oscillating period at the fundamental frequency is shown in Fig. 11 (turbulent and laminar flow snapshots have been plotted side-by-side for better comparison). The superposition of streamlines clearly identifies an evolving recirculation bubble set just upstream the GF, as well as the shedding of vortices into the wake. The mentioned recirculation bubble elongates and shortens cyclically along the airfoil wall over the period. Also the boundary layer separation on the airfoil upper-wall occurs in an oscillating manner. The visualization makes visible the appearance of a larger recirculating bubble ahead of the GF in the laminar flow simulation, which may explain the trend of having a smaller oscillating frequency when the turbulent diffusion is neglected in the simulation.

5.3 DMD on U-RANS datasets

The Ritz values μ_i have been calculated with eqn. (17) in Region-I of the wake (see Fig. 12a). They show that all the dynamic modes fell onto a unit circumference in the complex plane of the eigenvalues. The behaviour matches its counterpart, processed from the experiments and depicted in Fig. 12b. Then, the location of the eigenvalues agrees well with the quasi-periodical structures that evolve in the wake flow. It is noticed that no eigenvalue given by the U-RANS simulation occurs inside the circle (with the exception of a time-invariant mode at the origin of the diagram), thus any dynamic mode neither decays nor grows in time and then exhibits quasi-neutral stability. On the contrary, the experimental Ritz diagram shows that some

eigenvalues are located in the unit circle, which might be resulting from the contamination of measurement noise according to [35].

The projection of DMD modes onto a POD basis using eqns. (20-22) implies that the first dynamic modes comprise the large-scale coherent structures (and most of the energy), which drive the global flowfield. And the higher modes represent the small-scale turbulent structures. The modes amplitude (measured by the L_2-norm), which yields the energy content, is plotted in Fig. 13 for Regions I & II. Corresponding frequencies are obtained by normalization of ω_i by 2π, thus their actual values are recovered. The successive peaks correspond to the fundamental (f_0) and superharmonics ($2f_0$, $3f_0$, $4f_0$,...). The peaks indicate the decrease in energy as the frequency increases, which behaves monotonically in Region-I; but Region-II shows that there is greater energy content at $3f_0$ than at $2f_0$, which may be explained by the nonlinear interaction among modes as the structures are convected across both Regions I & II. A closer look at the spectrum points out that the major energy content is bounded below 5Hz, so the first 4 to 6 dynamic modes seem to be enough to describe the dominant dynamics involved. In particular, the root mean square error (RMSE) attained with only the four dominant modes (of the total of $r=21$ considered by the SVD truncation in the DMD algorithm), results to be RMSE~$O(10^{-4})$.
It is visible that opposite to the previous FFT analysis of the time-varying airfoil forces (see subsection 5.1), which provides the power energy lumped onto two frequencies (f_0, $2f_0$), the DMD analysis provides much richer detailed information regarding the flow spectrum.

The computed spatial patterns of the four dominant dynamic modes are compared side-by-side with their respective empirical ones using contour maps in Fig. 14, by applying the DMD algorithm to a sequence of snapshots of the v-component of the velocity in Regions I & II. The sequence examination indicates the presence of a hierarchy of descending scales embedded into the periodically convected vortices, with finer structures as they become higher-order harmonics. While the first and third modes show alternate-signed elliptical structures about the wake centreline, the second and fourth modes exhibit smaller-scale anti-symmetrical, alternate-signed elliptical structures about the centreline. It is visible in the sequence that the small-scale structures evolve quicker across the traverse direction than the larger ones.

Table 6 summarizes the frequency, wavelength and convection speed of these four dynamic modes. The streamwise wavelength is the length scale of the coherent structures, which is determined to be twice as long as the streamwise distance between the central locations of the positive and negative contributions.

It is observed an increase in frequency for each mode when the flow crosses from Region I to II. This frequency shift, greater for the superharmonics, is visible also in the energy spectrum depicted in Fig.13. The shift towards higher frequencies may be explained by the existence of a nonlinear interplay among lower and higher-frequency modes, which occurs during the convection of vortical structures downstream the wake. These major frequencies shift is clearly noticeable by means of the PIV-based dynamic modes, albeit the DMD analysis performed on the generated U-RANS datasets also identifies the frequencies increase, but in a weaker fashion. To clarify the origin of this weaker interplay obtained with U-RANS simulation, a more advanced simulation approach (i.e., Large Eddy Simulation or even DNS simulation), might be helpful to shed light on this phenomenon, but it is out of the scope of the present work. Finally, to mention that Table 6 shows that convection speed depends on the size of the structures, such that higher-order modes convect faster.

6. CONCLUSIONS

Understanding the vortex dynamics originated by an airfoil is fundamental to improving its performance. This investigation addresses the prediction and analysis of the incompressible turbulent flow at Re=10,300 in the presence of a Gurney flap device set on a NACA0015 airfoil. Following the delicate issue of identifying the best way to carry out the 2D U-RANS simulations in the OpenFOAM framework, the application of the data-driven DMD technique has permitted to capture very accurately the flow structures downstream the GF and vortex shedding into the wake, responsible for the quasi-periodical flowfield. This has been done by including the plausible blocking effect of the boundary layers along the walls of the water tunnel, as well as by an adequate turbulence characterization at the tunnel inlet. To the authors' knowledge, this study is the first that numerically focuses on the vortex shedding downstream a GF by using DMD to postprocess the data extracted from U-RANS simulations.

It is stressed that the conducted incompressible turbulent simulations based on the Reynolds averaging assumption exhibit a very accurate matching with the experiments in terms of reproducibility of the dominant experimental flow frequencies. Furthermore, the detailed numerical-experimental comparison provided by the DMD technique confirms the close prediction of the underlying flow dynamics and high-order harmonics. However, the issue of frequencies shifting underprediction during convection lacks a sound explanation and deserves further investigation. The results point out the cost-effective 2D U-RANS modelling as appropriate for this class of problems to generate the sequence of flow snapshots, out of which

successfully build a reduced-order representation of the flow dynamics. The presented approach reveals quite promising for those industrial oriented simulations which deal with lift-enhancement devices and lift-to-drag ratio optimization of airfoils, as it is the case in aeronautics, wind-power generation and the automotive industry, among others.

Acknowlegment

References

[1] Bai Z., Kaiser K., Proctor J.L, Kutz J.N., Brunton S.L. (**2020**): *Dynamic Mode Decomposition for Compressive System Identification*, AIAA Journal, Vol. 58 (2), pp. 561-574. DOI: 10.2514/1.J057870

[2] Rowley C.W., Dawson S.T.M. (**2017**): *Model Reduction for Flow Analysis and Control,* Annual Review in Fluid Mechanics Vol. 49, pp. 387-417. DOI: 10.1146/annurev-fluid-010816-060042

[3] Taira K. *et al.* (**2017**): *Modal Analysis of Fluid Flows: An Overview,* AIAA Journal, Vol. 55(12), pp. 4013-4041. DOI: 10.2514/1.J056060

[4] Brunton S.L., Kutz J.N. (**2019**): *Data-driven Science and Engineering*, Cambridge University Press (CUP) UK, ISBN 978-1-108-42209-3

[5] Higham J.E., Brevis W., Keylock C.J. (**2018**): *Implications of the Selection of a Particular Modal Decomposition Technique for the Analysis of Shallow Flows,* Journal of Hydraulic Research, Vol. 56(6), pp. 796–805. DOI: 10.1080/00221686.2017.1419990

[6] Semeraro O., Bellani G., Lundell F. (**2012**): *Analysis of Time-resolved PIV Measurements of a Confined Turbulent Jet using POD and Koopman Modes,* Exp. Fluids, Vol. 53, pp. 1203–1220

[7] Alenius E. (**2014**): *Mode Switching in a Thick Orifice Jet, an LES and Dynamic Mode Decomposition Approach,* Comput. Fluids, Vol. 90, pp. 101–112

[8] Liu Q., Luo Z., Deng X., Wang L., Zhou Y. (**2020**): *Numerical investigation on flow field characteristics of dual synthetic cold/hot jets using POD and DMD methods.* Chin. J. Aeronaut, Vol. 33, pp. 73–87.

[9] Montagnani D., Auteri F. (**2019**): *Non-modal Analysis of Coaxial Jets,* J. Fluid Mech., Vol. 872, pp. 665–696.

[10] Ayyappan D., Kumar A.S., Vaidyanathan A., Nandakumar K. (**2020**): *Study on Instability of Circular Liquid Jets at Subcritical to Supercritical Conditions Using Dynamic Mode Decomposition,* Phys. Fluids, Vol. 32, 014107.

[11] Li X.-R., Zhang X.-W., Hao P.-F., He F. (**2020**): *Acoustic Feedback Loops for Screech Tones of Underexpanded Free Round Jets at Different Modes,* J. Fluid Mech., Vol. 902, A17.

[12] Ayyappan D., Vaidyanathan A. (**2020**): *Study on Instability of Circular Liquid Jets at Subcritical to Supercritical Conditions using Dynamic Mode Decomposition,* Phys. Fluids, Vol. 32, 014107

[13] Schmid P.J., Li L., Juniper M.P., Pust O. (**2011**): *Application of the Dynamic Mode Decomposition,* Theor. Comput. Fluid Dyn. Vol. 25, pp. 249-259. DOI: 10.1007/s00162-010-0203-9

[14] Liu Y., Dong M., Fu B., Qiang L., Zhang C. (**2019**): *Direct Numerical Simulation of Fine Flow Structures of Subsonic-Supersonic Mixing Mayer,* Aerosp. Sci. Technol., Vol. 95, 105431.

[15] Cheng Y., Chen Q. (**2021**): *Large Eddy Simulation and Dynamic Mode Decomposition of Turbulent Mixing Layers*, Applied Sciences, Vol. 11(24), 12127. DOI: 10.3390/app112412127

[16] Nichols J.W., Larsson J., Bernardini M., Pirozzoli S. (**2017**): *Stability and Modal Analysis of Shock/Boundary Layer Interactions,* Theor. Comp. Fluid Dyn., Vol. 31, pp. 33–50.

[17] Waindim M., Agostini L., Larcheveque L., Adler M., Gaitonde D.V. (**2020**): *Dynamics of Separation Bubble Dilation and Collapse in Shock Wave/Turbulent Boundary Layer Interactions,* Shock Waves, Vol. 30, pp. 63–75.

[18] Pirozzoli S., Bernardini M., Marie S., Grasso F. (**2015**): *Early Evolution of the Compressible Mixing Layer Issued from Two Turbulent Streams,* J. Fluid Mech., Vol. 777, pp. 196–218.

[19] Lee J.H., Seena A., Lee S.-H., Sung H.J. (**2012**): *Turbulent Boundary Layers over Rod-and Cube-Roughened Walls,* J. Turbul., Vol. 13, N40.

[20] Garicano-Mena J., Li B., Ferrer E., Valero E. (**2019**): *A Composite Dynamic Mode Decomposition Analysis of Turbulent Channel Flows*, Phys. Fluids, Vol. 31, 115102. DOI: 10.1063/1.5119342

[21] Le Clainche, S.; Izbassarov, D.; Rosti, M.; Brandt, L.; Tammisola, O. (**2020**): *Coherent Structures in the Turbulent Channel Flow of an Elastoviscoplastic Fluid*, J. Fluid Mech., Vol. 888, A5.

[22] Noack B.R., Stankiewicz W., Morzynski M., Schmid P.J. (**2016**): *Recursive Dynamic Mode Decomposition of Transient and Post-transient Wake Flows,* J. Fluid Mech., Vol. 809, 843–872.

[23] De A.K.; Sarkar S. (**2020**): *Three-dimensional Wake Dynamics Behind a Tapered Cylinder with Large Taper Ratio,* Phys. Fluids, Vol. 32, 063604.

[24] Yin G., Ong M.C. (**2020**): *On the Wake Flow Behind a Sphere in a Pipe Flow at Low Reynolds Numbers,* Phys. Fluids, Vol. 32, 103605.

[25] Kumar P., Tiwari S. (**2019**): *Effect of Incoming Shear on Unsteady Wake in Flow Past Surface Mounted Polygonal Prism,* Phys. Fluids, Vol. 31, 113607.

[26] Loosen, S., Meinke, M., Schroeder, W. (**2020**): *Numerical Investigation of Jet-Wake Interaction for a Dual-Bell Nozzle,* Flow Turbul. Combust., Vol. 104, pp. 553–578.

[27] Jang H.K., Ozdemir C.E., Liang J.H. (**2021**): *Oscillatory Flow Around a Vertical Wall-mounted Cylinder: Dynamic Mode Decomposition,* Phys. Fluids, Vol. 33, 025113. DOI: 10.1063/5.0032644

[28] Li-Hao Feng, Jin-Jun Wang, Chong Pan (**2011**): *Proper Orthogonal Decomposition Analysis of Vortex Dynamics of a Circular Cylinder under Synthetic Jet Control,* Phys. Fluids, Vol 23, 014106 (2011) https://doi.org/10.1063/1.3540679

[29] Lusseyran F., Guéniat F., Basley J., Douay C., Pastur L., Faure T., Schmid P., (**2011**): *Flow Coherent Structures and Frequency Signature: Application of the Dynamic Modes Decomposition to Open Cavity Flow,* J. Phys.: Conf. Ser. 318, 042036

[30] Basley J., Pastur L.R., Delprat N., Lusseyran F. (**2013**): *Space-time Aspects of a Three-dimensional Multi-modulated Open Cavity Flow,* Phys. Fluids, Vol. 25, 064105

[31] Vinha N., Meseguer-Garrido F., De Vicente J., Valero E. (**2016**): *A Dynamic Mode Decomposition of the Saturation Process in the Open Cavity Flow,* Aerosp. Sci. Technol., Vol. 52, pp. 198–206

[32] Seena A., Sung H.J. (**2011**): *Dynamic Mode Decomposition of Turbulent Cavity Flows for Self-sustained Oscillations,* International Journal of Heat Fluid Flow, Vol. 32(6), pp.1098–1110. DOI: 10.1016/j.ijheatfluidflow.2011.09.008

[33] Schmid P.J., Meyer K.E., Pust O. (**2009**): *Dynamic Mode Decomposition and Proper Orthogonal Decomposition of Flow in a Lid-driven Cylindrical Cavity*, in Procs. 8th Int. Symp. on Particle Image Velocimetry (PIV09), August 25-28, Melbourne, Australia.

[34] Srinivasan G., Mahapatra S., Sinhamahapatra K.P., Ghosh S. (**2020**): *Dynamic Mode Decomposition of Supersonic Turbulent Pipe Flow with and without Shock Train*, J. Turbul., Vol. 21, pp. 1–16

[35] Pan C., Yu D., Wang J. (**2011**): *Dynamical Mode Decomposition of a Gurney flap Wake Flow*, Theor. Appl. Mech. Lett., Vol. 1, pp. 012002.1-012002.5. DOI: 10.1063/2.1101202

[36] Nonomura T., Koki Nankai K., Iwasaki Y., Komuro A., Asai K. (**2021**): *Quantitative Evaluation of Predictability of Linear Reduced-order Model Based on Particle-Image-Velocimetry Data of Separated Flow Field Around Airfoil*, Experiments in Fluids, Vol. 62,112. DOI: 10.1007/s00348-021-03205-8

[37] Neumann P. *et al.* (**2021**): *Reduced Order Modelling for Plasma Aeroelastic Control of Airfoils in Cascade: Dynamic Mode Decomposition*. In: Braza M., Hourigan K., Triantafyllou M. (eds.) Advances in Critical Flow Dynamics Involving Moving/Deformable Structures with Design Applications. Notes on Numerical Fluid Mechanics and Multidisciplinary Design (NNFM series), Vol. 147, Springer, DOI: 10.1007/978-3-030-55594-8_21

[38] Wang J., Kim K.C. (**2019**): *Wake/Shear Layer Interaction for Low-Reynolds-number Flow over Multi-element Airfoil*, Experiments in Fluids, Vol. 60(16), DOI: 10.1007/s00348-018-2662-5

[39] Liebeck R.H. (**1978**): *Design of Subsonic Airfoils for High Lift*, J. Aircraft, Vol.15(9), pp. 547-561

[40] Alber J. *et al.* (**2020**): *Aerodynamic Effects of Gurney Flaps on the Rotor Blades of a Research Wind Turbine*, Wind Energ. Sci., Vol. 5, pp.1645–1662. DOI: 10.5194/wes-5-1645-2020

[41] Alber J. *et al.* (**2021**): *Experimental Investigation of Mini Gurney Flaps in Combination with Vortex Generators for Improved Wind Turbine Blade Performance.* Wind Energ. Sci., Preprint. DOI: 10.5194/wes-2021-124

[42] Zhang Y., Ramdoss V., Saleem Z., Wang X., Schepers G. Ferreira C. (**2019**): *Effects of Root Gurney Flaps on the Aerodynamic Performance of a Horizontal Axis Wind Turbine.* Energy, Vol. 187, 115955. DOI: 10.1016/j.energy.2019.115955

[43] Aramendia I., Fernandez-Gamez U., Zulueta E., Saenz-Aguirre A., Teso-Betoño D. (**2019**): *Parametric Study of a Gurney Flap Implementation in a DU91W(2)250 Airfoil,* Energies, Vol. 12, 294. DOI: 10.3390/en12020294

[44] Houghton E.L., Carpenter P.W., Collicott S.H., Valentine D.T. (**2017**): *Flow Control and Wing Design*, *Aerodynamics for Engineering Students*, 7th Ed. (Chapter 10), Butterworth-Heinemann, Elsevier Ltd., USA. ISBN: 978-0-08-100194-3

[45] Basso M., Cravero C., Marsano D. (**2021**): *Aerodynamic Effect of the Gurney Flap on the Front Wing of a F1 Car and Flow Interactions with Car Components*, Energies, Vol. 14, 2059. DOI: 10.3390/en14082059

[46] Stalewski W. (**2018**): *Flow Control on Helicopter-rotor Blades Via Active Gurney Flap*, Transactions of the Institutte of Aviation, Vol.1, pp. 98-118. DOI: 10.2478/tar-2018-0007.

[47] Doerffer P., Barakos G.N., Marcin M. Luczak M.M. (eds.) (**2017**): *Recent Progress in Flow Control for Practical Flows*, Springe, Switzerland. ISBN 978-3-319-50567-1

[48] Tiainen J., Grönman A., Jaatinen-Värri A., Backman A. (**2018**): *Flow Control Methods and Their Applicability in Low-Reynolds-Number Centrifugal Compressors - A Review*, Int. J. Turbomach. Propuls. Power, Vol. 3(2). DOI: 10.3390/ijtpp3010002

[49] Feng L.H., Choi K.S., Wang J.J. (**2015**): *Flow Control over an Airfoil Using Virtual Gurney Flaps*, J. Fluid Mech., Vol. 767, pp. 595-626. DOI: 10.1017/jfm.2015.22

[50] Richter K.E. (**2009**): *Untersuchungen zur Aerodynamik von Miniature Trailing-Edge Devices in Transsonischen Strömungen*, Doctoral Thesis D-82, Diss. RWTH Aachen University, Germany.

[51] Suresh M., Sitaram N. (**2011**): *Gurney Flap Applications for Aerodynamic Flow Control*, in Procs. Int. Conf. Mechanical Engineering (ICME2011), ICME11-FL-040, 18-20 Dec., Dhaka, Bangladesh.

[52] Meena M.G., Taira K., Asai K. (**2018**): *Airfoil-Wake Modification with Gurney flap at Low Reynolds Number*, AIAA J., Vol. 56 (4), pp. 1348–1359. DOI: 10.2514/1.J056260

[53] Schatz M., Günther B., Thiele F. (**2004**): *Computational Modeling of the Unsteady Wake behind Gurney-Flaps*, AIAA Paper 2004-2417, in Procs. 2nd AIAA Control Conference, 28 June - 1 July, Portland, Oregon, USA.

[54] Troolin D.R., Longmire E.K., Lai W.T. (**2006**): *The Effect of Gurney Flap Height on Vortex Shedding Modes Behind Symmetric Airfoils*, in Procs. 13th Int. Symp. Applications of Laser Techniques to Fluid Mechanics, Lisbon, Portugal, 26-29 June.

[55] www.openfoam.com/documentation/user-guide

[56] He G., Wang J., Pan C., Feng L., Gao Q., Rinoshika A. (**2017**): *Vortex Dynamics for Flow Over a Circular Cylinder in Proximity to a Wall,* Journal of Fluid Mechanics Vol. .812, pp. 698-720. DOI:10.1017/jfm.2016.812

[57] Wang J.J., Pan C., Zhang P.Z. (**2009**): *On the Instability and Reproduction Mechanism of a Laminar Streak,* J. Turbulence, Vol.10(26), pp. 1-27:, DOI: 10.1080/14685240902906127

[58] Pan C., Wang J., Zhang C. (**2009**): *Identification of Lagrangian Coherent Structures in a Turbulent Boundary Layer*, Science in China Series G: Physics Mechanics and Astronomy, Vol. 52(2), pp. 248-257, DOI: 10.1007/s11433-009-0033-1

[59] Behrens T. (**2018**): *OpenFOAM's Basic Solvers for Linear Systems of Equations*, Report, 18 pages, Dept. Applied Mechanics, Chalmers TU, Sweden.

[60] Hanjalić K., Launder B.E. (**2020**): *Eddy-Viscosity Transport Modelling: A Historical Review*. In Procs. 50 Years of CFD in Engineering Sciences, Runchal A. (ed.), Springer Nature Singapore Pte Ltd. DOI: 10.1007/978-981-15-2670-1_9

[61] Leschziner M., Drikakis D. (**2002**): *Turbulence Modelling and Turbulent Flow Computation in Aeronautics,* The Aeronautical Journal, 106 (1061), pp. 349-384. DOI: 10.1017/S0001924000092137

[62] Launder B.E., Sharma B.I. (**1974**): *Application of the Energy-Dissipation Model of Turbulence to the Calculation of Flow Near a Spinning Disc*, Letters in Heat and Mass Transfer, Vol. 1, pp. 131-138.

[63] Lien F.S., Leschziner M. A. (**1993**): *A Pressure-Velocity Solution Strategy for Compressible Flow and its Application to Shock/Boundary-layer Interaction Using Second-moment Turbulence Closure*, Journal of Fluids Engineering, Vol. 115(4), pp. 717-725. DOI: 10.1115/1.2910204

[64] Lam C.K.G., Bremhorst K. (**1981**): *A Modified Form of the k-ε Model for Predicting Wall Turbulence*, Journal of Fluids Engineering, Vol. 103(3), pp. 456-460.

[65] Lien F.S., Chen W.L. Leschziner M.A. (**1996**): *Low-Reynolds-number Eddy-viscosity Modeling Based on Non-linear Stress-Strain/Vorticity Relations*, Engineering Turbulence Modelling and Experiments, Vol. 3, pp. 91-100. DOI: 10.1016/B978-0-444-82463-9.50015-0

[66] Menter F.R., Kuntz M., Langtry R. (**2003**): *Ten Years of Industrial Experience with the SST Turbulence Model.* In Procs. Turbulence, Heat and Mass Transfer 4 (Eds.: Hadjalić *et al.*)

[67] Bardina J.E., Huang P.G., Coakley T.J. (**1997**): *Turbulence Modelling Validation, Testing and Development.* NASA TM 110446, 98 pages, Ames Rerearch Centre, USA.

[68] Poroseva S., Iaccarino G. (**2001**): *Simulating Separated Flows Using the k-ε Model.* Stanford Center for Turbulence Research, Annual Research Briefs, pp. 375-383, Stanford, USA.

[69] Weaver D.S., Mišković S. (**2021**): *A Study of RANS Turbulence Models in Fully Turbulent Jets: A Perspective for CFD-DEM Simulations,* Fluids, Vol. 6, 271. DOI: 10.3390/fluids608027

[70] Moradnia P., Chernoray V.G., Nilsson H. (**2011**): *Experimental and Numerical Investigation of the Cooling Air FLow in an ELectric Generator.* In Procs. HEFAT2011, 8th International Conference on Heat Transfer, Fluid Mechanics and Thermodynamics, p. 242-249.

[71] Rodríguez Pascual M.A., Moríñigo J.A., Mayo-García R. (**2019**): *Effect of MPI Tasks Location on Cluster Throughput Using NAS*, Cluster Computing, Vol. 22(4), pp. 1187-1198.

[72] Bai Z., Kaiser K., Proctor J.L, Kutz J.N., Brunton S.L. (**2020**): *Dynamic Mode Decomposition for Compressive System Identification,* AIAA Journal, Vol. 58 (2), pp. 561-574. DOI: 10.2514/1.J057870

[73] Rowley C.W., Dawson S.T.M. (**2017**): *Model Reduction for Flow Analysis and Control,* Annual Review in Fluid Mechanics, Vol. 49, pp. 387-417. DOI: 10.1146/annurev-fluid-010816-060042

[74] Taira K. *et al.* (**2017**): *Modal Analysis of Fluid Flows: An Overview,* AIAA Journal, Vol. 55(12), pp. 4013-4041. DOI: 10.2514/1.J056060

[75] Brunton S.L., Kutz J.N. (**2019**): *Data-driven Science and Engineering*, Cambridge University Press, United Kingdom, ISBN 978-1-108-42209-3

[76] Tu J.H., Rowley C.W., Luchtenburg D.M., Brunton S.L., Kurts J.N (**2014**): *On Dynamic Mode Decomposition: Theory and Applications,* J. Computational Dynamics, Vol. 1(2), pp. 391-421. DOI: 10.3934/jcd.2014.1.391

[77] Trefethen L.N., Bau D.I. (**1997**): *Numerical Linear Algebra* (chapter 11), SIAM, Philadelphia, USA.

TABLES

Table 1: Baseline grid sizing of both computational domains corresponding to the free-flight airfoil and water tunnel domain. Structured grid has been built in the boundary layers (over the airfoil and flat walls of the water tunnel), as well as in the data-extraction Regions I & II (see Fig. 5).

Domain zone	Number of cells	
	Free-fligth airfoil	Water tunnel
Structured gridded - hexahedra (BLs[1], Regions I & II)	106,631 [2]	125,767 [2]
Unstructured gridded - prisms	113,504	110,931
Total	220,135	236,698

[1] BLs: Boundary layers. The water tunnel domain, besides the BL on the airfoil, has a BL on the tunnel walls.

[2] The extra 19,136 hexahedral cells in the water tunnel domain are due to the gridding in the nearby the tunnel walls.

Table 2: Series of U-RANS simulations performed with the water tunnel domain. Slip-flow BC and Non-slip-flow BC have been imposed on the tunnel flat walls to explore the blocking effect of the BCs (slip-flow BC vs. non-slip-flow BC) on the computed flow spectrum. The three types of gridding in the nearby of the walls correspond to the views shown in Fig. 6. The BC type indicated in each simulation is linked to a combination of the flow modelling (laminar/turbulent) with a grid type.

Flow modelling	Type of gridding near the water tunnel walls		
	Baseline Grid #1	Hexahedra-cells by BL[1] Grid #2	Prism-cells by BL[1] Grid #3
Laminar	Non-slip-flow BC	Non-slip-flow BC	Slip-flow BC[2]
Turbulent (U-RANS) with Launder & Sharma EVM	Non-slip-flow BC	— [3]	Slip-flow BC[2]

[1] This BL refers to the boundary layer on the water tunnel flat walls.

[2] The slip-flow BC treats the tunnel flat wall as a symmetry surface.

[3] The BL by the tunnel flat wall is too coarse to satisfy $y^+\sim1$ with the EVMs.

Table 3: Prediction of major frequencies found in the drag coefficient with laminar and turbulent (Launder & Sharma EVM) flow modelling. Results correspond to the free-flight airfoil and the water tunnel computational domains (two different BCs are considered at the water tunnel walls: non-slip-flow and slip-flow).

Computational domain & BCs	Flow modelling	Frequencies[1]	
		Fundamental (Hz)	Second (Hz)
Free-flight airfoil	Laminar	0.51	1.02
	Turbulent	0.61	1.21
Water tunnel Slip-flow BCs (Grid #3)	Laminar	0.53	1.04
	Turbulent	0.62	1.24
Water tunnel Non-slip-flow BCs (Grid #1)	Laminar	0.55	1.10
	Turbulent	0.64	1.28

[1] Experimental values: fundamental frequency = 0.65 Hz , second frequency = 1.31 Hz

Table 4: Prediction of lift (C_L) and drag (C_D) coefficients obtained with the four k-ε turbulence models in the water tunnel computational domain (Grid #1). The laminar case is added for comparison purposes (mean value plus/minus the oscillation range are provided for each case).

	Turbulent flow modelling				
	Launder & Sharma	Lam & Bremhorst	Lien & Leschziner	NLEVM Lien *et al.*	Laminar
C_L	0.0126 ± 0.0129	0.0126 ± 0.0128	0.0127 ± 0.0125	0.0126 ± 0.0129	0.0127 ± 0.0134
C_D	0.0531± 0.0002	0.0528± 0.0002	0.0528± 0.0002	0.0527± 0.0002	0.0536± 0.0002

Table 5: Insensitivity of the major frequencies found in the drag coefficient, computed with low-Reynolds k-ε linear and non-linear EVMs and water tunnel computational domain (Grid #1).

U-RANS closure	Frequencies		Error (%)[1]
	Fundamental (Hz)	Second (Hz)	
Launder & Sharma	0.638	1.276	1.85
Lam & Bremhorst	0.641	1.282	1.38
Lien & Leschziner	0.635	1.270	2.31
NLEVM[2] Lien *et al*.	0.644	1.288	0.92

[1] Numerical-experimental error: $100 \cdot (f_{exp} - f_{num})/f_{exp}$

[2] NEVM: non-linear eddy viscosity model

Table 6: Frequency, wavelength and convection velocity (in nondimensional form, c/U_∞) of the four most dominant dynamic modes, postprocessed from the experiments [35] and U-RANS simulation (notice that a third decimal place is provided in the numerical frequencies to better quantify the shift between Regions I & II).

	f_o		$2f_o$		$3f_o$		$4f_o$	
	Region I	Region II	Region I	Region II	Region I	Region II	Region I	Region II
Experiments (time resolved PIV datasets)								
$\omega_i/2\pi$ (Hz)	0.65	0.68	1.29	1.36	1.94	2.01	2.59	2.68
λ (mm)	58.2	65.4	31.4	36.6	22.4	24.1	17.8	18.5
c/U_∞	0.73	0.86	0.78	0.96	0.84	0.93	0.89	0.95
Numerical simulation (CFD datasets)								
$\omega_i/2\pi$ (Hz)	0.636	0.641	1.272	1.282	1.910	1.923	2.549	2.560
λ (mm)	54.5	71.3	29.4	37.7	21.0	25.0	16.8	20.2
c/U_∞	0.67	0.88	0.72	0.93	0.77	0.92	0.82	0.99

FIGURES
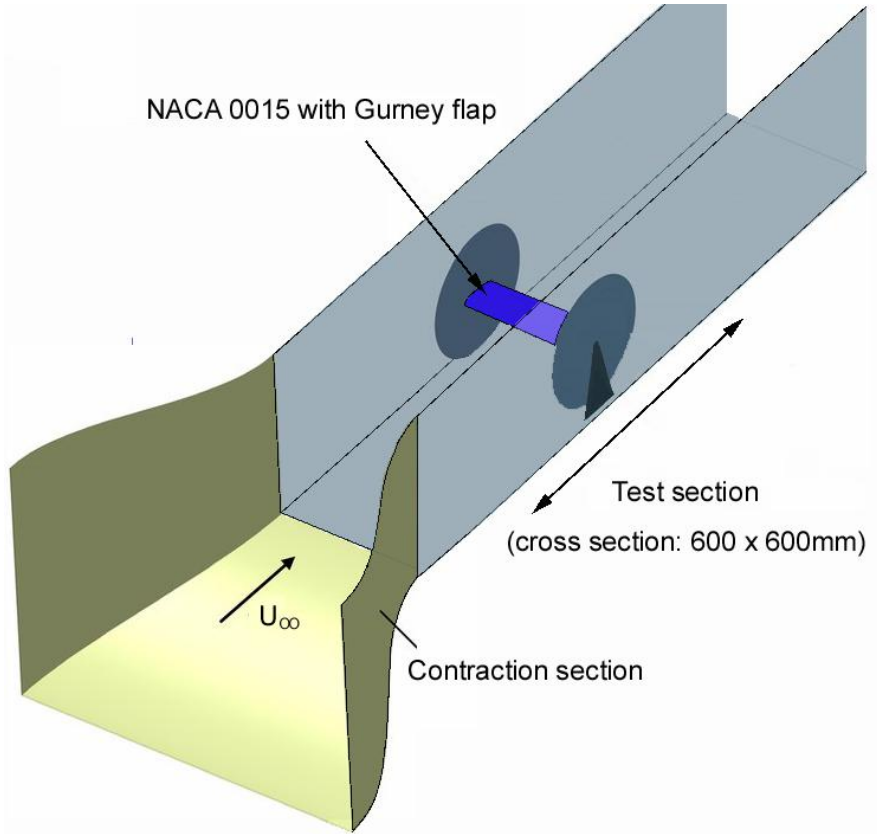
Fig. 1: Sketch of the water tunnel facility with the airfoil placed at the test section of dimensions 600 x 600 x 3000mm.
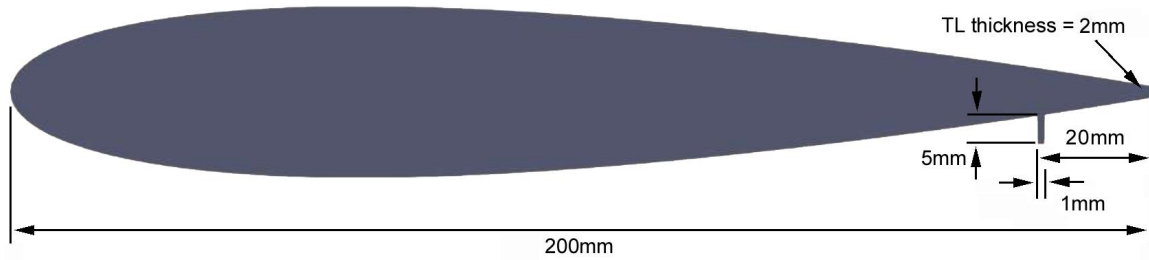
Fig. 2: Geometry of airfoil NACA0015 modified with a Gurney flap set at 10% of the airfoil chord by the trailing edge (dimensions in millimeters. Airfoil chord is 200mm).
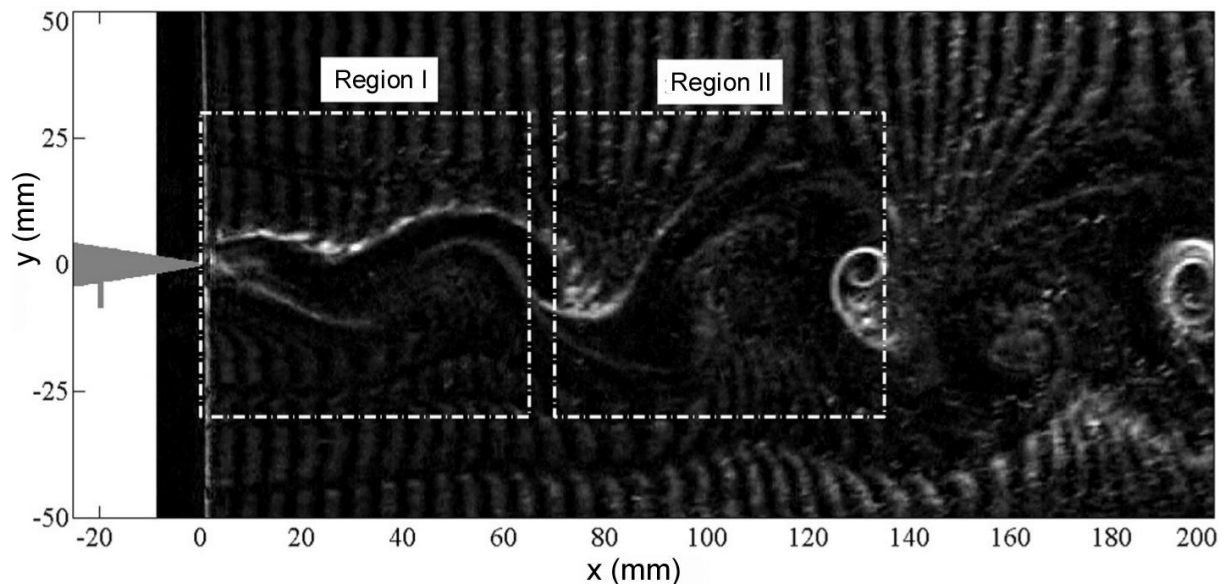
28

Fig. 3: Hydrogen bubbles based visualization of the time-evolving flowfield downstream the airfoil, where the vortices shed into the wake are clearly visible. The two dashed boxes (labeled Region I and II) correspond to the PIV data regions, sized according to the field of view of the PIV camera. The rear portion of the airfoil with the GF is shown in solid grey on the left (re-elabored from [35]).
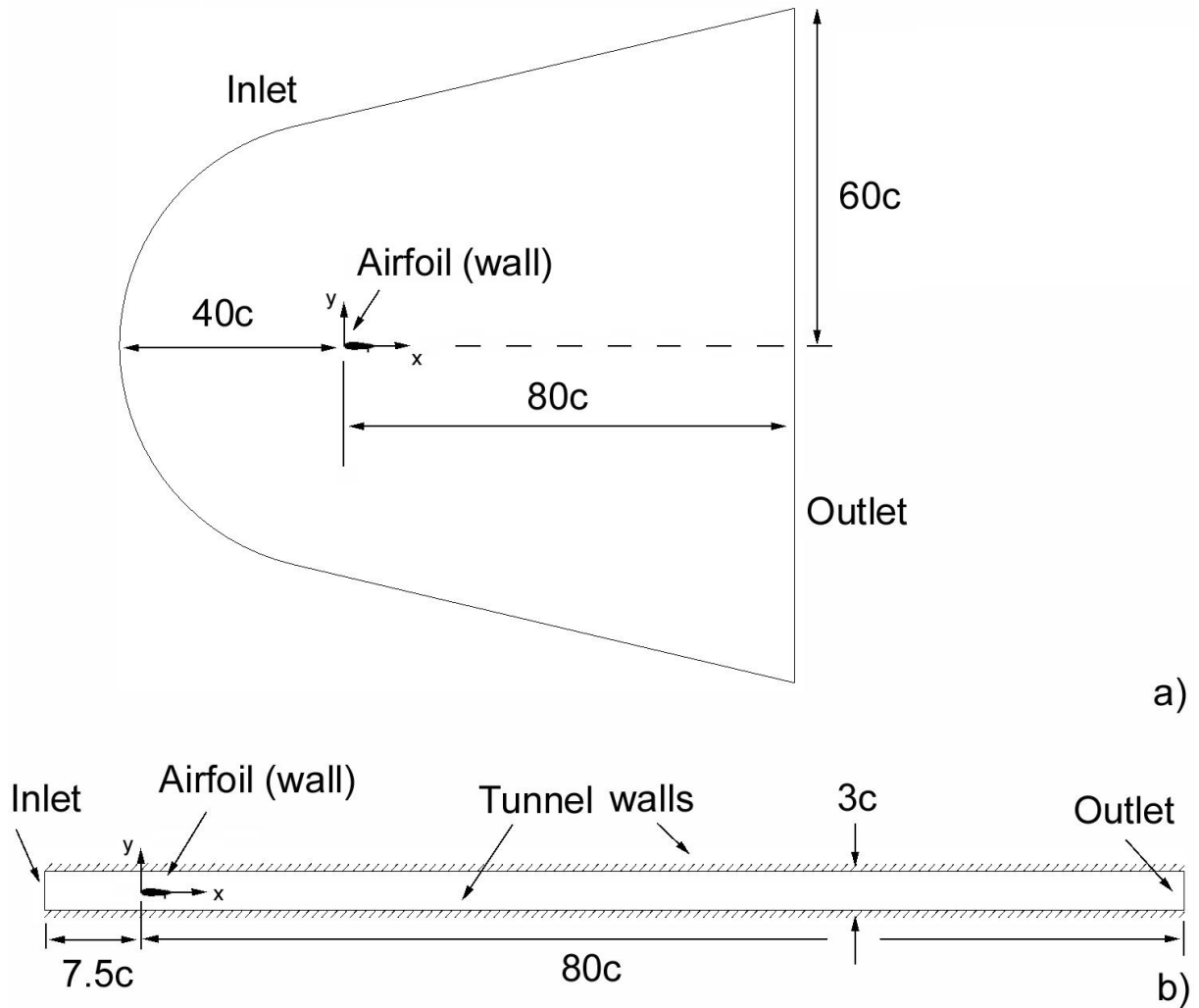
Fig. 4: Layout of the computational domains: a) Free-flight airfoil; b) Confined airfoil in a water tunnel, mimicking the test facility. Boundary conditions and relative dimension (as multiples of the chord c) are indicated. Coordinate axis are set at the leading edge of the airfoil.
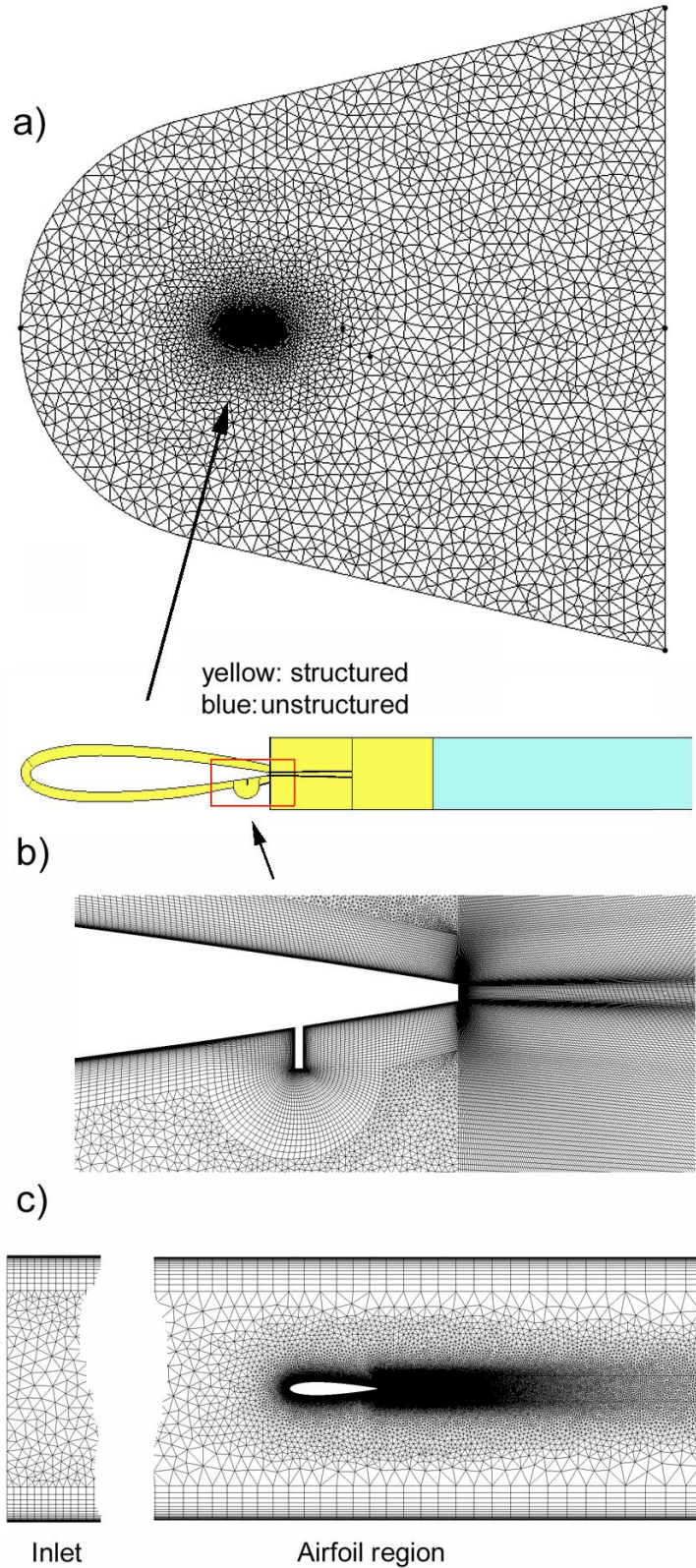
Fig. 5: Grids of the two computational domains: a) Gridded free-flight airfoil; b) Structured blocking by the airfoil and wake zone, to ensure the grid quality around the airfoil (notice that this topological blocking and grid around the airfoil and close wake are identical for both computational domains). A zoomed view of the grid in the vicinity of the GF and TE is shown; c) Inlet and airfoil regions of the water tunnel computational domain.
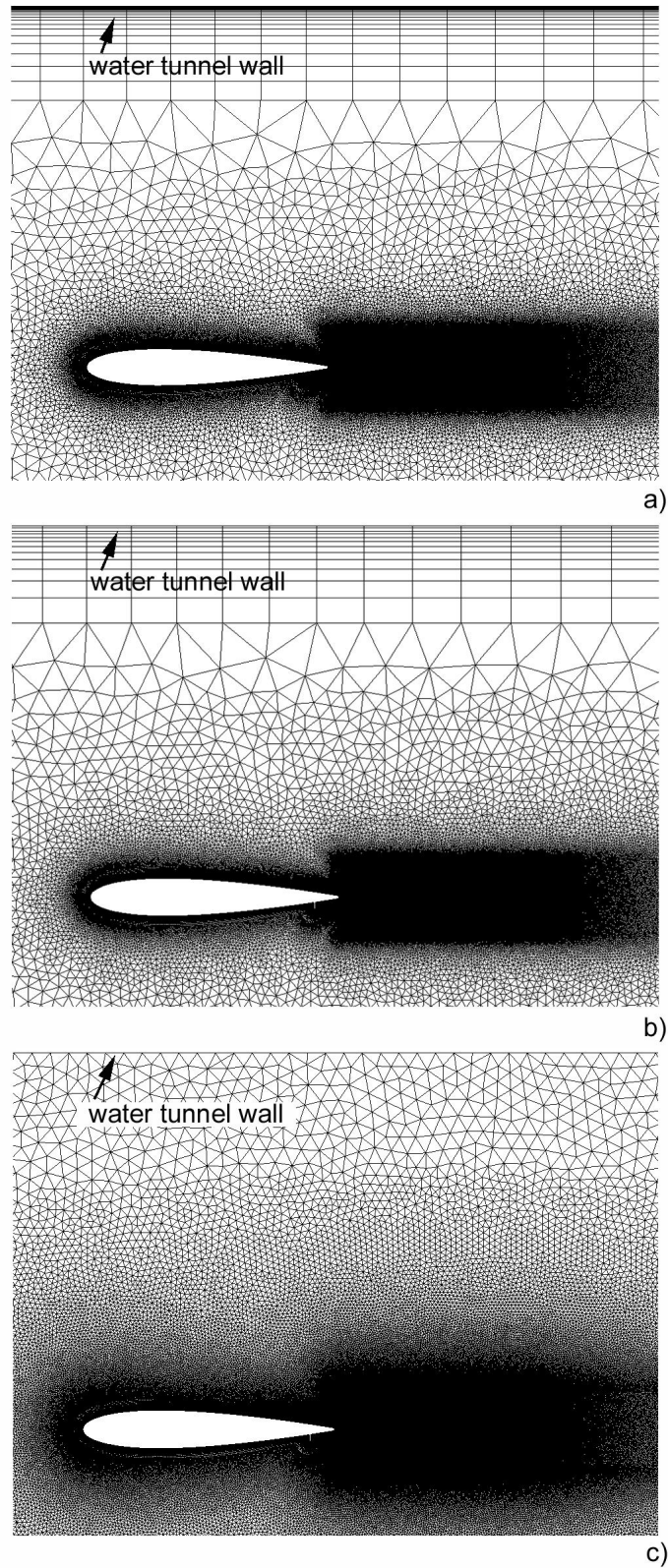
Fig. 6: Three grids of the water tunnel computational domain, where the zone close to the tunnel wall is gridded in a different way: a) Baseline grid (Grid #1) as shown in Fig. 5b-c; b) Coarser hexahedra-cells by the wall, intended for laminar simulation (Grid #2); c) Isotropic prism-cells near the wall, intended for laminar and turbulent simulation with a slip-flow BC set on the tunnel flat walls (Grid #3).
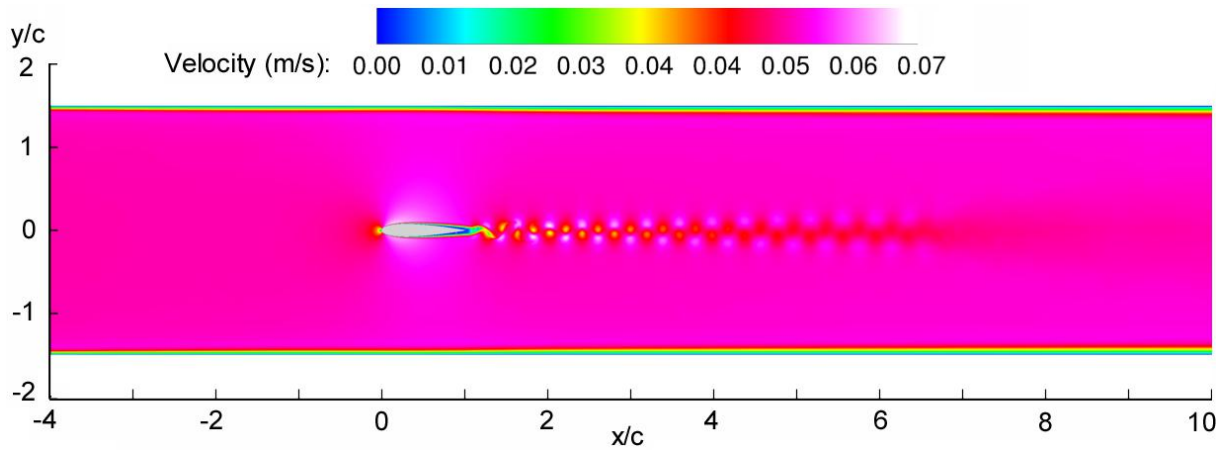
Fig. 7: View of the vortex street developed in the water tunnel domain. The velocity flowfield corresponds to a generic time instant of the U-RANS simulation performed with the Launder & Sharma EVM (coordinates are non-dimensionalized with the airfoil chord *c*).
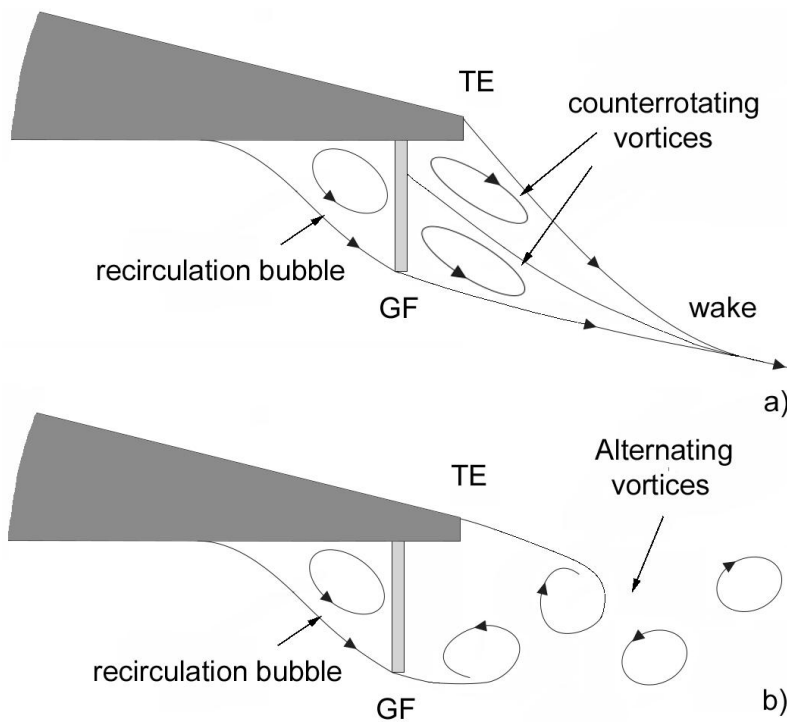
Fig. 8: Layout of two feasible vortex patterns downstream the GF and TE: a) Counterrotating vortices at low Reynolds number; b) Von Kármán street at higher Reynolds number. A coupling exists between the fluctuations in the downstream zone and the recirculating, "breathing" bubble ahead of the GF.
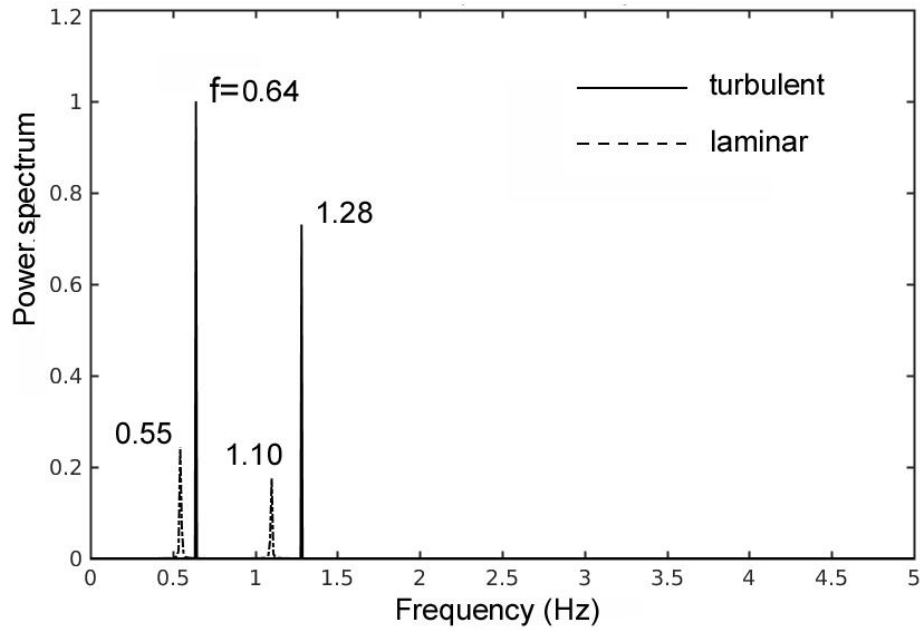
Fig. 9: Power spectrum of the drag coefficient, computed for the water tunnel domain with laminar and turbulent (EVM of Launder & Sharma) flow modeling and non-slip-flow BCs set at the water tunnel walls. Spectrum peaks corresponding to the fundamental frequency (f_0) and second harmonic ($2f_0$) are labeled with their values (both spectra are non-dimensionalized with the maximum value of the turbulent case).
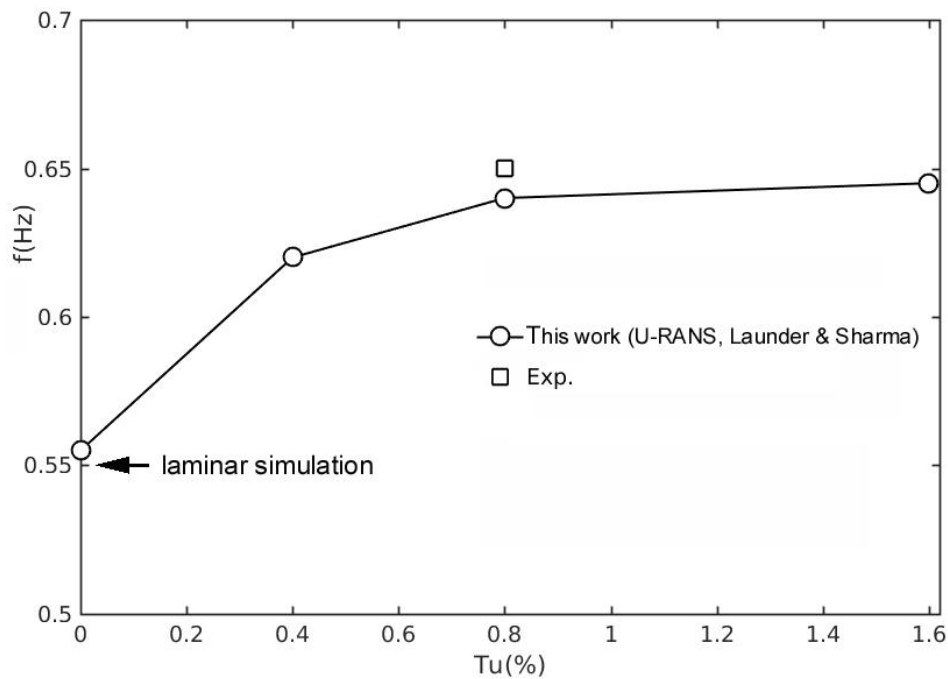

Fig. 10: Sensitivity of the drag coefficient major frequency to the turbulence intensity prescribed at the inlet of the water tunnel domain. The results of U-RANS simulation with Tu(%)=0, 0.4, 0.8 (baseline) and 1.6 are plotted. The fundamental frequency 0.55Hz obtained with laminar flow modelling is indicated.
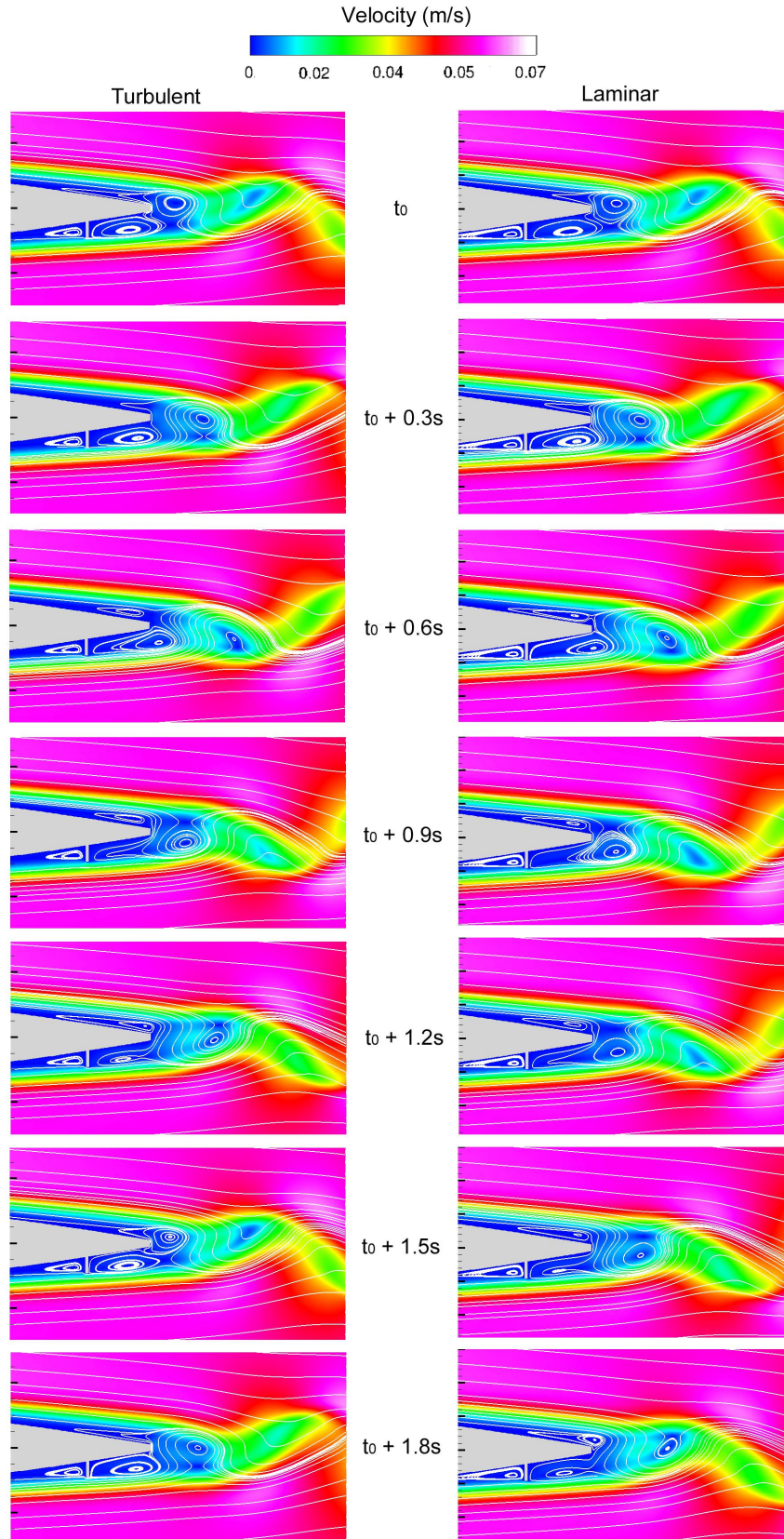
Fig. 11: Time-evolving flowfield near the airfoil TE computed with turbulent (left column) and laminar (right column) flow modelling. The sequence comprises aproximately one period at the fundamental frequency (time between snapshots: 0.3 seconds, being t_0 a generic instant). Streamlines are plotted to visualize the fluid separation, recirculation bubble ahead of the GF and vortex shedding into the wake.
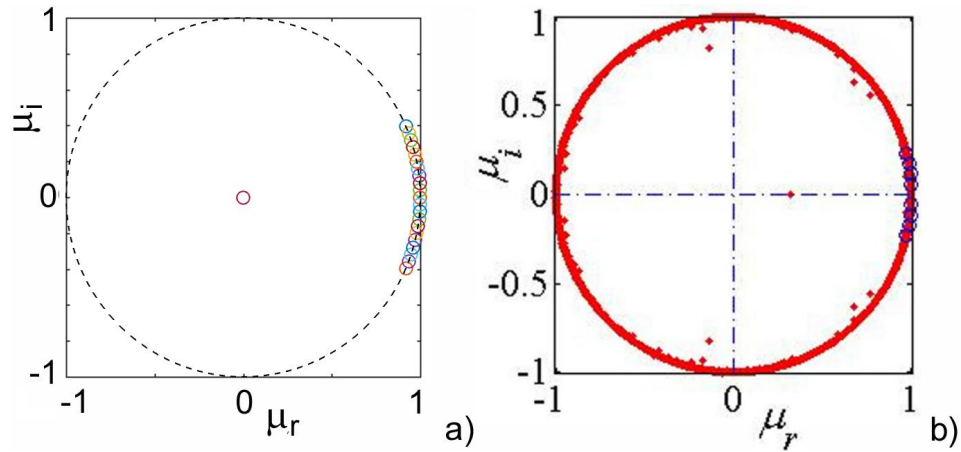
Fig. 12: Ritz diagram of Region I: a) First twenty-one eigenvalues of the dynamic modes (red circles) computed from CFD data; b) Eigenvalues computed from time-resolved PIV data (blue circles correspond to the first four dominant dynamic modes. Taken from [35]).
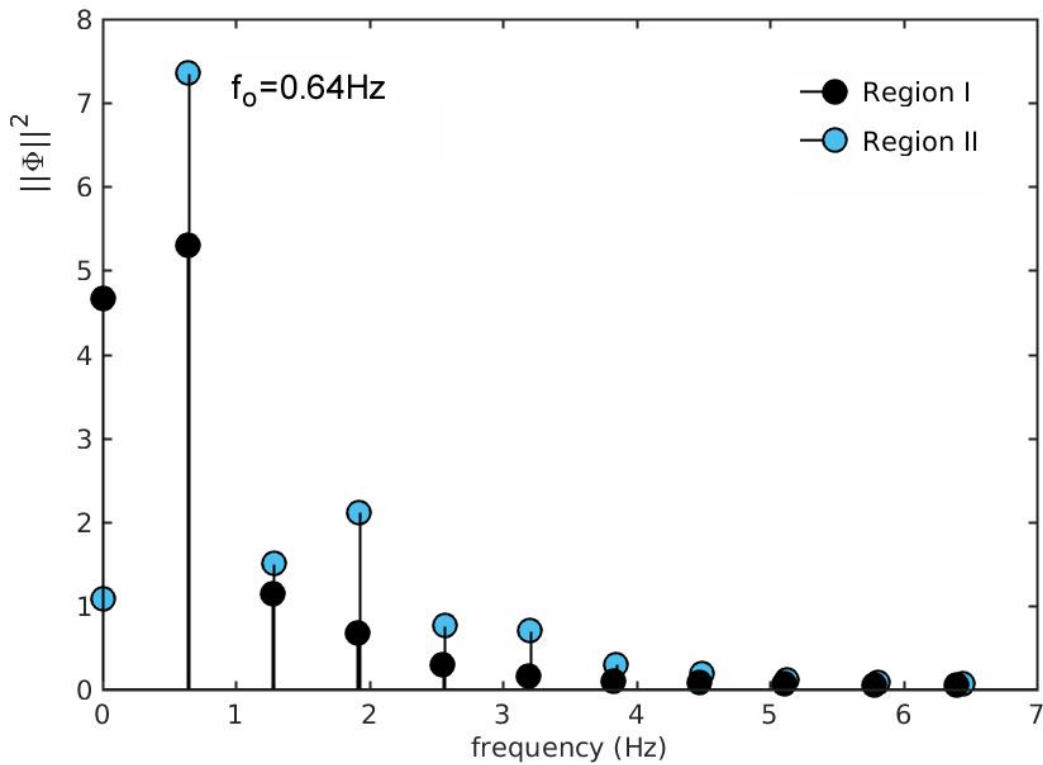

Fig. 13: Decay of the DMD modes energy, computed in Regions I & II from the CFD datasets. The fundamental $f_o=0.64$Hz is indicated. A paulatine shift of the corresponding frequencies in Regions I & II is visible.
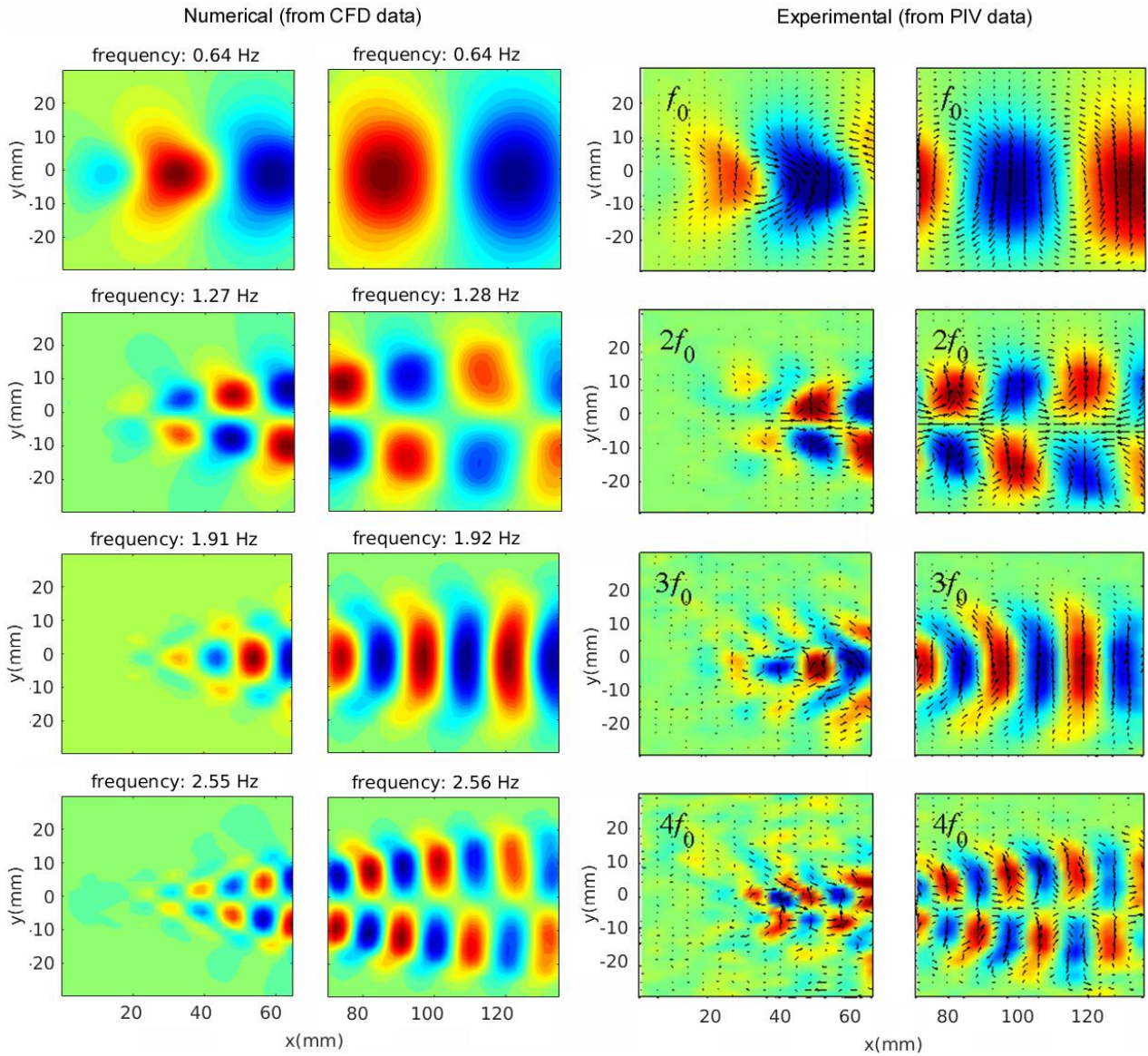
Fig. 14: Spatial patterns of the four dominant dynamic modes processed from the v-component of the fluid velocity (u,v) in Regions I & II: DMD from CFD data (left column); and DMD from PIV measurement (right column, re-elabored from [35]), with velocity vectors superimposed. Rows correspond to frequencies f_0 (fundamental), $2f_0$, $3f_0$ and $4f_0$.